https://doi.org/10.5194/egusphere-2026-6876
Preprint. Discussion started: 12 November 2026
© Author(s) 2026. CC BY 4.0 License.

Aerosol Hygroscopic Growth as a Key Driver of Aerosol-Radiation Interactions in Radiation Fog

Hao Ding[1,2], Alejandro Baró Pérez[1,2], Nazario Mastroianni[1,2,3], Almuth Neuberger[2,3,4], Rahul Ranjan[2,3,5], Fredrik Mattsson[2,3], Liine Heikkinen[2,3], Karam Mansour[6], Stefano Decesari[6], Angelo Lupi[7], Claudia Mohr[2,3,8,9], Paul Zieger[2,3], Ilona Riipinen[2,3], and Annica M. L. Ekman[1,2]

[1]Department of Meteorology, Stockholm University, Stockholm, Sweden
[2]Bolin Centre for Climate Research, Stockholm, Sweden
[3]Department of Environmental Science, Stockholm University, Stockholm, Sweden
[4]now at: Institute for Hygiene and Environment, Hamburg State Institute for Food Safety, Health Protection and Environmental Investigations, Hamburg, Germany
[5]now at: Department of Technical Physics, Faculty of Science, Forestry and Technology, University of Eastern Finland, Kuopio, Finland
[6]Institute of Atmospheric Science and Climate, National Research Council of Italy, Bologna, Italy
[7]Institute of Polar Sciences, National Research Council of Italy, Bologna, Italy
[8]now at: Center for Energy and Environmental Sciences, Paul Scherrer Institute, Villigen, Switzerland
[9]now at: Department of Environmental Systems Science, ETH Zurich, Zurich, Switzerland

Correspondence: Hao Ding (hao.ding@misu.su.se) and Annica M. L. Ekman (annica.ekman@misu.su.se)

Abstract.

Aerosol–radiation interactions (ARI) can alter the thermodynamic structure of the atmospheric boundary layer and thereby influence the evolution of radiation fog. Previous modeling studies have focused primarily on the shortwave radiative effect of aerosols and often assumed aerosols to be dry when interacting with radiation ("dry ARI"), neglecting the role of aerosol water in modifying particle size, optical properties, and longwave radiative transfer ("wet ARI"). Here, we use a large-eddy simulation model with explicit representations of dry aerosols, wet aerosols, and activated cloud droplets to systematically explore their radiative effects on a wintertime radiation fog case observed during the FAIRARI campaign in the Po Valley, Italy. The simulations show that the radiative effect of aerosols is weak if the aerosols are assumed to be dry. In contrast, the fog development is highly sensitive to the radiative effects of wet aerosols. Wet ARI enhances longwave radiative cooling at the fog top, strengthening in-fog turbulent mixing, promoting droplet activation, and increasing the vertical extent of the fog. This leads to a larger fog optical depth and stronger attenuation of shortwave radiation, resulting in improved agreement with observations of surface radiative fluxes and fog persistence. Increasing the accumulation-mode aerosol number concentration (5,000-25,000 cm^{-3}) generally enhances fog geometric height, optical depth, and liquid water path, effects that become substantially more pronounced when wet ARI are considered. Within the observed range of aerosol chemical composition, aerosol hygroscopicity (κ = 0.33-0.53) is the dominant chemical factor shaping the fog life cycle, while variations in black carbon content have a negligible effect. These results highlight the important role of wet ARI in understanding long-term fog trends and their responses to aerosol changes.

https://doi.org/10.5194/egusphere-2026-6876
Preprint. Discussion started: 12 November 2026
© Author(s) 2026. CC BY 4.0 License.

1 Introduction

The Po Valley in Italy is one of the most polluted regions in Europe, as the semi-enclosed basin topography favors accumulation of aerosols within the boundary layer (BL). At the same time, moisture is frequently transported to the area by air masses from the Mediterranean Sea. During autumn and winter, persistent high-pressure systems accompanied by weak winds often lead to high aerosol loadings and frequent occurrences of radiation fog, posing major hazards to transport safety and human health (Putaud et al., 2014; Decesari et al., 2017; Egli et al., 2019; Di Antonio et al., 2023; Pauli et al., 2024; Neuberger et al., 2025a). The formation and evolution of radiation fog result from complex interactions between cloud microphysical processes, thermodynamics, and dynamics, including nonlinear feedbacks involving aerosols, radiation, and turbulence. Aerosols primarily influence radiation fog through two physically distinct but strongly coupled pathways, both of which are highly uncertain. The first is aerosol–cloud interaction (ACI), wherein aerosols act as cloud condensation nuclei (CCN), modifying fog microphysics by affecting droplet activation and thereby the droplet size distribution. Previous studies have shown that higher aerosol loadings increase droplet number concentration and liquid water content, leading to thicker fog layers and prolonged fog duration (Bott et al., 1990; Stolaki et al., 2015; Maalick et al., 2016; Ding et al., 2026). The second is aerosol-radiation interaction (ARI), wherein aerosols alter atmospheric radiative transfer through processes such as scattering and absorption of shortwave radiation, thereby modifying the thermal structure and turbulent mixing within the BL. For instance, during daytime, aerosols reduce incoming solar radiation and surface heat fluxes, causing near-surface cooling, while absorbing aerosols can heat the upper BL. This weakens buoyancy-driven turbulence, suppresses BL growth and vertical mixing, and consequently promotes the accumulation of aerosols near the surface (Bond et al., 2013; Gao et al., 2015; Ding et al., 2016; Petäjä et al., 2016; Slater et al., 2020; Yan et al., 2021).

However, the specific impacts of ARI on radiation fog behavior remain unclear. Some modeling studies indicate that accounting for the radiative effects of absorbing aerosols within the BL, compared to a scenario without any ARI, significantly delays the dissipation of radiation fog by warming the upper fog layer and cooling the surface, thereby strengthening the temperature inversion and suppressing turbulence (Arun et al., 2025). In contrast, Anurose et al. (2024) studied a fog hole event over the Indo-Gangetic Plain and reported that the absorbing aerosols warmed the whole BL, delaying fog formation and accelerating fog dissipation. Moreover, the relative importance of ARI and ACI in fog is uncertain. For instance, ARI was shown to exert a substantially stronger impact than ACI on the formation of widespread advection-radiation fog over eastern China; aerosol absorption stabilized the BL, resulting in near-surface cooling and moistening (Ding et al., 2019). In contrast, for another widespread fog under highly polluted conditions over eastern China, the response of fog evolution to increasing aerosol concentrations was dominated by ACI, with ARI playing only a minor role (Yan et al., 2021). Similarly, Arun et al. (2025) found that, for a mixed advection-radiation fog event over the Indo-Gangetic Plain, ACI accounted for approximately 84% of the prolongation of fog duration caused by enhanced aerosol loading, whereas ARI contributed only about 16% and primarily during daytime. These uncertainties in understanding ARI result partly from differences in meteorological conditions, pollution levels, and aerosol chemical composition among the various fog events investigated in the aforementioned studies. Here, we would like to highlight that differing results may also be obtained due to different model treatments of aerosol hygroscopic

https://doi.org/10.5194/egusphere-2026-6876
Preprint. Discussion started: 12 November 2026
© Author(s) 2026. CC BY 4.0 License.

growth and associated radiative effects. In most studies, aerosol radiative effects have typically been considered only for dry aerosol particles, while the hygroscopic growth of aerosols and its influence on longwave radiation has not been explicitly represented. Consequently, a substantial number of unactivated wet aerosols have been overlooked in terms of their radiative effect. In high-humidity radiation fog, aerosol particle sizes can increase by several times under hygroscopic growth, leading to significant changes in their optical properties such as single-scattering albedo and extinction coefficient (Hammer et al., 2014; Elias et al., 2015; Neuberger et al., 2025b; Nguyen et al., 2016). This could alter the magnitude or even the sign of the aerosol radiative effect, further affecting radiative transfer, BL thermodynamic structure, and the fog life cycle.

Given the above background, this study aims to systematically investigate the role of ARI and how changes in aerosol physicochemical properties influence the life cycle of radiation fog. We use the large-eddy simulation (LES) MISU–MIT Cloud and Aerosol (MIMICA) model to simulate a case of radiation fog observed during the Fog and Aerosol Interaction Research Italy (FAIRARI) 2021/2022 field campaign (Neuberger et al., 2025a). MIMICA has previously been shown to reasonably reproduce this specific fog event (Neuberger et al., 2025b; Ding et al., 2026). Building on this framework, we have further developed the aerosol module in MIMICA so that it explicitly represents aerosol hygroscopic growth and its coupling with the shortwave and longwave part of the radiation scheme. With this setup, we can examine aerosol impacts on radiation and fog properties when aerosols are considered to be completely dry when interacting with the radiation ("dry ARI") or when hygroscopic growth of the aerosols and aerosol water influences the radiation ("wet ARI"). The following questions will be addressed:

1) How important is aerosol hygroscopic growth and aerosol water in shaping the fog life cycle, i.e., the fog microphysics, radiative properties, and vertical structure?
2) How sensitive is the fog behavior to accumulation-mode aerosol loading when dry ARI or wet ARI are considered?
3) How do the fog properties respond to variations in aerosol chemical composition when dry ARI or wet ARI are considered, particularly in terms of aerosol hygroscopicity and absorbing aerosol content?

2 Data and methods

2.1 Model description

MIMICA is a large-eddy simulation model that solves the non-hydrostatic, anelastic governing equations (Savre et al., 2014). The exchange of momentum, heat, and moisture between the surface and the atmosphere are parameterized under prescribed surface forcing conditions based on Monin–Obukhov similarity theory (Stull, 1988). Cloud microphysics is represented using a two-moment bulk scheme (Seifert and Beheng, 2001, 2006), which in its default configuration accounts for microphysical processes such as collision–coalescence and autoconversion. Hydrometeor size distributions are described by gamma functions, from which droplet sedimentation in the Stokes regime can be calculated (Bergot, 2016; Contreras Osorio et al., 2022; Ding et al., 2026). Supersaturation treatment follows the pseudo-analytical approach that allows the integration of condensation/evaporation terms over each time step (Morrison and Grabowski, 2008). MIMICA also includes a two-moment interactive aerosol scheme, in which all aerosol modes are represented by lognormal size distributions (Ekman et al., 2006). Aerosol hygroscopic growth and activation are solved based on κ-Köhler theory (Petters and Kreidenweis, 2007). Hydrometeors and

https://doi.org/10.5194/egusphere-2026-6876
Preprint. Discussion started: 12 November 2026
© Author(s) 2026. CC BY 4.0 License.

aerosols are coupled to a four-stream radiative transfer scheme with six shortwave and twelve longwave bands (Fu and Liou, 1993; Fu et al., 1997; Gu et al., 2003), in which aerosols are assumed to be internally and homogeneously mixed within each mode, such that the mean complex refractive index of the aerosol mixture is determined from the volume-fraction-weighted refractive indices of individual chemical components (Baró Pérez et al., 2024), as well as aerosol water uptake when wet ARI is enabled. The wavelength-dependent refractive indices of aerosol species from Bond and Bergstrom (2006) and Slater et al. (2020) are listed in Table S1 in the Supplementary Information. Based on these, the aerosol radiative parameters and optical properties, including optical thickness, single-scattering albedo, and phase functions, can be computed and incorporated into the four-stream radiation scheme (Baró Pérez et al., 2024).

2.2 Simulation setup

The simulated case consisted of three consecutive radiation fog events observed at the San Pietro Capofiume (SPC) site in Italy during the FAIRARI campaign on 18–19 February 2022 (Neuberger et al., 2025a). All simulations started at 18:00 local standard time (LST) and ended at 14:00 LST the next day. The reference simulation setup in this study largely followed that of Ding et al. (2026), and key configurations are summarized in Table 1. The simulation domain covered 0.16 km × 0.16 km × 1.6 km, with grid cells of 5 m × 5 m × 2 m. The initial meteorological profiles were prescribed based on SPC radiosonde observations and ECMWF Reanalysis (ERA5, Hersbach et al., 2023). Surface temperature and moisture forcing were prescribed using the 3.5-m observations. This type of setup allowed us to isolate the influence of atmospheric ARI on the formation and evolution of the radiation fog.

Aerosol concentrations were, as a default, assumed to be vertically uniform. Their size distribution was obtained from a single-mode lognormal fit to the observed mean dry aerosol spectrum during the fog events, measured by a Differential Mobility Particle Sizer (DMPS) over a diameter range of 13.3–792 nm (Neuberger et al., 2025a; Karlsson et al., 2022), with a total number concentration of 5,000 cm^{-3}, a geometric mean radius of 48.2 nm, and a dimensionless geometric standard deviation of 1.9. The aerosol chemical composition was prescribed according to the observed mean of the fog event, measured by a Soot Particle Aerosol Mass Spectrometer (SP-AMS) (Neuberger et al., 2025a; Onasch et al., 2012), with a bulk hygroscopicity parameter κ = 0.45, calculated using the Zdanovskii–Stokes–Robinson (ZSR) method (Stokes and Robinson, 1966). The droplet size distribution was represented by a gamma distribution fitted to the observed mean droplet spectrum, measured by a Ground-based Fog and Aerosol Spectrometer (GFAS), with shape parameters α = 3 and ν = 1. Building on the conclusions of Neuberger et al. (2025b) and Ding et al. (2026) regarding the dominant microphysical processes governing radiation fog evolution, a simplified microphysical process representation was adopted in this study. Specifically, for aerosols, hygroscopic growth, activation, and turbulent transport were enabled, while nucleation scavenging and regeneration through hydrometeor evaporation were disabled due to the very low aerosol activation fraction. For fog droplets, key processes included condensation/evaporation, turbulent transport, and sedimentation, while the collision–coalescence process was neglected given the small droplet sizes and low collision efficiency. Additionally, drizzle formation was excluded since no precipitation was observed.

A time step of approximately 1.0 second was used for dynamic and microphysical process calculations to capture the rapid temporal evolution of supersaturation and associated fog microphysical development. Due to the high computational cost of

https://doi.org/10.5194/egusphere-2026-6876
Preprint. Discussion started: 12 November 2026
© Author(s) 2026. CC BY 4.0 License.

the radiative transfer solver and relatively small temporal variability of the radiative properties, radiation calculations were performed every 60.0 seconds.

Under the identical model configurations described above, three reference simulations were conducted using different ARI representations. In the first reference simulation, only hydrometeors were coupled with radiation, while aerosols did not affect radiative transfer; this simulation was therefore labeled as REF_NoARI. In the second, radiative effects of both hydrometeors and aerosols were included, but the aerosol water uptake did not influence the radiation calculations; this simulation was labeled as REF_DryARI. The third reference simulation accounted for the radiative effects of hydrometeors, dry aerosols, and wet aerosols, and was labeled as REF_WetARI. The corresponding ARI representations are hereinafter referred to as NoARI, DryARI, and WetARI.

Table 1. Summary of the model setup for the reference simulations. Please see the main text for a more detailed description.

Category	Parameter/process configuration
Simulation domain	[X × Y × Z] = [160 × 160 × 1600] m; [Δ x × Δ y × Δ z] = [5 × 5 × 2] m
Simulation timestep	Dynamics and microphysics solver ∼ 1.0 s; Radiation solver ∼ 60.0 s
Aerosol input	LogNormal (N_a = 5,000 cm^{-3}, r_g = 48.2 nm, σ = 1.9); bulk κ = 0.45
Aerosol processes	Activation, Hygroscopic growth, Turbulent transport
Droplet size distribution	$\Gamma(\alpha = 3, \nu = 1)$
Droplet processes	Condensation/Evaporation, Sedimentation, Turbulent transport
Radiation coupling	REF_NoARI: Hydrometeors ON, Dry aerosols OFF, Wet aerosols OFF REF_DryARI: Hydrometeors ON, Dry aerosols ON, Wet aerosols OFF REF_WetARI: Hydrometeors ON, Dry aerosols ON, Wet aerosols ON

2.3 Sensitivity experiments

Building on the reference simulations in Sect. 2.2, and to examine the response of fog properties to changes in aerosol number concentration (N_a) when dry and wet ARI are considered, a series of sensitivity experiments was further conducted for all three reference simulations, with N_a increased from 5,000 cm^{-3} to 25,000 cm^{-3} in increments of 5,000 cm^{-3}, covering typical pollution levels observed in the Po Valley from the 1980s to the present (Noone et al., 1992; Neuberger et al., 2025a). For each N_a level, simulations were performed under all three ARI scenarios, denoted as Na*_NoARI, Na*_DryARI, and Na*_WetARI, respectively.

In addition to aerosol loading, aerosol chemical composition can also modify aerosol hygroscopic growth and optical properties during the fog evolution. To isolate the intrinsic direct radiative effects of individual aerosol components, a set of idealized simulations was designed. With aerosol activation disabled, that is, in the absence of fog formation, the reference aerosol mixture was replaced by pure black carbon (BC), sulfate (SULF), sea salt (SALT), and organic aerosol (OA), respectively. For each aerosol type, simulations were performed for all three ARI scenarios and are denoted as Pure*_NoARI, Pure*_DryARI, and Pure*_WetARI, respectively. A differencing approach was applied to quantify the contributions of each component. For a given aerosol type, the difference between Pure*_DryARI and Pure*_NoARI represents the direct radiative effect of dry aerosols;

https://doi.org/10.5194/egusphere-2026-6876
Preprint. Discussion started: 12 November 2026
© Author(s) 2026. CC BY 4.0 License.

the difference between Pure*_WetARI and Pure*_DryARI corresponds to the radiative effect arising solely from aerosol hygroscopic growth; and the difference between Pure*_WetARI and Pure*_NoARI represents the total radiative effect of both dry and wet aerosols. These idealized experiments are intended to assess the contributions of different aerosol components to the ARI, with detailed results provided in Sect. S2 in the Supplementary Information.

The idealized experiments indicate that that longwave radiation is mainly affected by wet aerosols, with a negligible effect from dry aerosols, whereas the effect on shortwave radiation comes almost entirely from BC (Fig. S1). Since these two factors (hygroscopicity and BC content) act on different aspects of the radiation budget, their impacts on ARI can be considered approximately decoupled; that is, the impact of each can be independently investigated with the other one being held fixed. Accordingly, two sets of sensitivity experiments focusing on aerosol chemical composition were designed based on observed values. In the first set, the bulk hygroscopicity parameter (κ) was fixed at the reference value of 0.45, while the BC volume fraction was prescribed as the 0th, 25th, 50th, 75th, and 100th percentiles observed during the FAIRARI campaign; the corresponding simulations for different ARI conditions are denoted as BC*p_NoARI, BC*p_DryARI, and BC*p_WetARI. In the second set, the BC volume fraction was fixed at the reference value of 2.0%, with κ being varied according to its 0th, 25th, 50th, 75th, and 100th percentile values in the observations; these simulations are correspondingly denoted as K*p_NoARI, K*p_DryARI, and K*p_WetARI. For each target BC or κ level, the Sequential Least Squares Programming (SLSQP) method was employed to optimize the proportions of the remaining aerosol components to yield a chemical composition that satisfies the above constraints while maintaining a total volume fraction of 100%. The resulting aerosol chemical compositions are provided in Sect. S3. Apart from changes in chemical composition, all other model settings remain identical to those of the reference simulations under each respective ARI condition. A summary of all experiment configurations is presented in Table. 2.

Table 2. Summary of sensitivity and idealized experiments. Key parameters include aerosol number concentration (N_a), aerosol chemical composition, aerosol activation (OFF indicates exclusion of ACI), and different levels of aerosol-radiation interaction.

Experiment category	Simulation label	N_a (cm^{-3})	Chemical composition	Aerosol activation	DryARI	WetARI
Reference simulations	REF_NoARI	5,000	Reference mixture	ON	OFF	OFF
	REF_DryARI	–	–	ON	*ON	OFF
	REF_WeARI	–	–	ON	*ON	*ON
Sensitivity to N_a	Na*_NoARI	*10,000; 15,000; 20,000; 25,000	–	ON	OFF	OFF
	Na*_DryARI	*10,000; 15,000; 20,000; 25,000	–	ON	ON	OFF
	Na*_WetARI	*10,000; 15,000; 20,000; 25,000	–	ON	ON	ON
Sensitivity to BC content	BC*p_NoARI	–	*BC = [P_0, P_{25}, P_{50}, P_{75}, P_{100}] from Obs.	ON	OFF	OFF
	BC*p_DryARI	–	*BC = [P_0, P_{25}, P_{50}, P_{75}, P_{100}] from Obs.	ON	ON	OFF
	BC*p_WetARI	–	*BC = [P_0, P_{25}, P_{50}, P_{75}, P_{100}] from Obs.	ON	ON	ON
Sensitivity to aerosol hygroscopicity	K*p_NoARI	–	*κ = [P_0, P_{25}, P_{50}, P_{75}, P_{100}] from Obs.	ON	OFF	OFF
	K*p_DryARI	–	*κ = [P_0, P_{25}, P_{50}, P_{75}, P_{100}] from Obs.	ON	ON	OFF
	K*p_WetARI	–	*κ = [P_0, P_{25}, P_{50}, P_{75}, P_{100}] from Obs.	ON	ON	ON
Idealized experiments	Pure*_NoARI	–	*pure [BC, SULF, SALT, OA]	OFF	OFF	OFF
	Pure*_DryARI	–	*pure [BC, SULF, SALT, OA]	OFF	ON	OFF
	Pure*_WetARI	–	*pure [BC, SULF, SALT, OA]	OFF	ON	ON

https://doi.org/10.5194/egusphere-2026-6876
Preprint. Discussion started: 12 November 2026
© Author(s) 2026. CC BY 4.0 License.

2.4 Key parameters for the analysis

- The simulated *fog geometric height H* is determined from grid cells satisfying both an activated cloud droplet number concentration $N_{c,act} \geq 1\,\mathrm{cm}^{-3}$ and a corresponding liquid mixing ratio $Q_{c,act} \geq 0.01\,\mathrm{g\,kg}^{-1}$, following the criterion of Maronga and Bosveld (2017). The lowest and highest levels that meet these conditions are defined as the *fog base* and *fog top*, respectively.

- The *liquid water path LWP* is calculated as the integral of liquid water content (LWC) of activated droplets within the fog layer:

$$\mathrm{LWP} = \int_{\text{fog base}}^{\text{fog top}} \rho_{air}(z)\, Q_{c,act}(z)\, dz, \tag{1}$$

and the *fog optical thickness* τ is expressed as:

$$\tau = \frac{3\,\mathrm{LWP}}{2\,\rho_w\, r_{\mathrm{eff}}}, \tag{2}$$

where ρ_w is the density of liquid water, ρ_{air} is the air density, and r_{eff} is the droplet effective radius (Morrison and Grabowski, 2007; Brenguier et al., 2011).

- The near-surface (averaged over the lowest 5 m) *total fog droplet number concentration* N_c includes both *hydrated particles* $N_{c,hyd}$ and *activated droplets* $N_{c,act}$. Consistent with the low detection threshold commonly used in fog monitors (Neuberger et al., 2025b), particles with wet diameters larger than 2 µm are classified as fog droplets, among which particles exceeding the activation diameter are counted as activated droplets, whereas those exceeding 2 µm but remaining below the activation size are categorized as hydrated particles.

- The near-surface *visibility Vis*, accounting for both hydrated particles larger than 2 µm and activated droplets, is parameterized following Gultepe et al. (2006):

$$\mathrm{Vis} = \frac{1.002}{(\mathrm{LWC}\cdot N_c)^{0.6473}} = \frac{1.002}{(\rho_{air} Q_c \cdot N_c)^{0.6473}}, \tag{3}$$

Simulated *fog periods* are defined by a Vis ≤ 1 km and RH $\geq 90\%$ (Neuberger et al., 2025a), and the first and last time points meeting these criteria are identified as *fog onset* and *fog dissipation times*, respectively.

- The *aerosol hygroscopic growth factor, HGF*, which is calculated based on κ-Köhler theory, is defined as the ratio of wet to dry particle diameters:

$$\mathrm{HGF} = \frac{D_{wet}}{D_{dry}}. \tag{4}$$

https://doi.org/10.5194/egusphere-2026-6876
Preprint. Discussion started: 12 November 2026
© Author(s) 2026. CC BY 4.0 License.

The HGF is used to calculate the *mixing ratio of aerosol liquid water uptake* Q_{aw}, given by:

$$Q_{aw} = \frac{\pi}{6}\rho_w N_a \left(D_{wet}^3 - D_{dry}^3\right)/\rho_{air} = \frac{\pi}{6}\rho_w N_a D_{dry}^3 \left(HGF^3 - 1\right)/\rho_{air}, \tag{5}$$

where N_a is the total aerosol number concentration.

– The *longwave radiative rate DT_LW* is the vertical divergence of *net longwave radiation flux FRAD_LW*:

$$DT_LW = \left(\frac{\partial T}{\partial t}\right)_{\mathrm{LW}} = -\frac{1}{\rho_{air} c_p}\frac{\partial FRAD_LW}{\partial z}, \tag{6}$$

where c_p is the specific heat capacity of air at constant pressure. The *shortwave (DT_SW)* and *total (DT_TOT) radiative rates* are calculated analogously from *net shortwave (FRAD_SW)* and *total (FRAD_TOT) radiation fluxes*, respectively.

3 Results and discussion

3.1 Comparison of reference simulations

Fig. 1 shows time–height cross-sections of the fog for the three reference simulations with different ARI configurations. Overall, the in-fog pattern is broadly consistent across the simulations, and all of them reproduce the typical features of radiation fog evolution. Specifically, surface and longwave radiative cooling drives the near-surface air toward supersaturation with respect to water vapor, leading to aerosol activation and fog initiation (Bergot, 2013; Maronga and Bosveld, 2017). As the geometric and optical thickness of the fog increases, the area of high supersaturation and droplet number shift upward from the surface toward the fog top. After sunrise (at around 07:01 LST), droplet evaporation driven by surface warming causes the fog layer to decouple from the surface and eventually dissipate (Price, 2011; Ding et al., 2026).

https://doi.org/10.5194/egusphere-2026-6876
Preprint. Discussion started: 12 November 2026
© Author(s) 2026. CC BY 4.0 License.

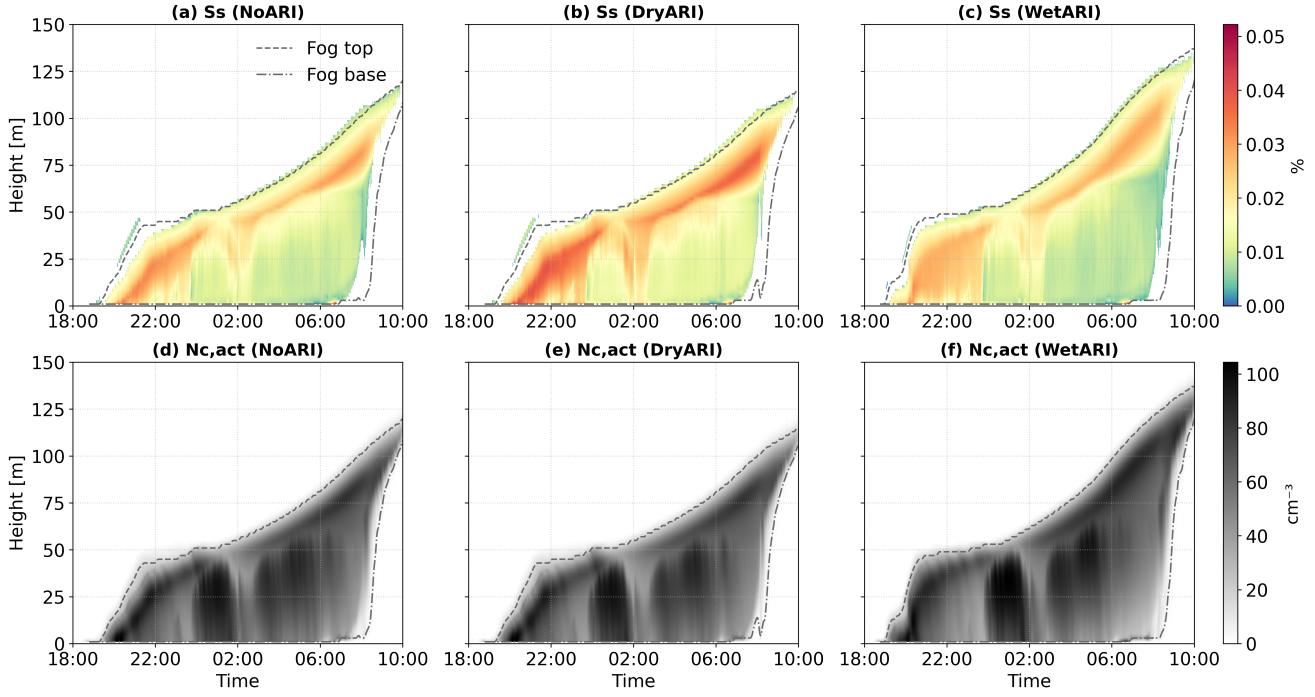


Figure 1. Time–height cross-sections of horizontally averaged (a-c) supersaturation (Ss) and (d-f) number concentration of activated droplets (Nc, act) in the reference simulations with different ARI representations.

However, despite an overall consistent evolution in the three simulations, the structural properties of the fog exhibit pronounced differences. In terms of vertical development, the fog-top lifting rate is highest throughout the fog period in WetARI, while the rates in NoARI and DryARI (Fig. 2a) are comparable. The evolution of the fog optical depth (τ) and liquid water path (LWP) does not fully follow the same pattern as the geometric height, instead showing distinct time-dependent discrepancies (Fig. 2b, 2c). This discrepancy is primarily attributed to the development and shifting dominance between the fog-top layer and the mixed layer during fog evolution. The fog-top layer is characterized by a strong temperature inversion ($> 0.1\,\mathrm{K\,m^{-1}}$) and decreasing longwave radiative cooling with height, whereas the mixed layer is characterized by increasing longwave radiative cooling with height and enhanced turbulent mixing compared to the fog-top layer (e.g., Fig. 3a_ii, b_ii, c_ii). Accordingly, and following Ding et al. (2026), the fog life cycle is divided into three stages: the formation period (P1, 19:00–22:00 LST), the surface warming period (P2, 22:00–02:00 LST), and the subsequent period until fog dissipation (P3, 02:00–08:00 LST), as shown in Fig. 2.

During the fog formation stage P1, the relatively low optical thickness of the fog leads to weak negative buoyancy and turbulent mixing in the simulations, and the fog vertical structure is largely dominated by radiative cooling within the fog-top layer (Fig. 3a_i). Compared with the other simulations, the optical thickness under WetARI is higher, resulting in a more pronounced vertical gradient in the longwave radiation fluxes (Fig. 3d_i) and stronger radiative cooling (Fig. 3b_i, see also Eq. 6), which enhances local supersaturation and aerosol activation (Fig. 3e_i, 3f_i). At this stage, the near-surface net longwave radiation

https://doi.org/10.5194/egusphere-2026-6876
Preprint. Discussion started: 12 November 2026
© Author(s) 2026. CC BY 4.0 License.

flux in WetARI agrees well with observations, whereas the other two ARI scenarios both show a substantial underestimate (Fig. 3d_i). Meanwhile, the stronger radiative cooling in WetARI compared to the other two simulations increases the hygroscopic growth factor and aerosol water uptake (Fig. 3h_i), which, together with the increasing number of activated droplets, enhances longwave radiative cooling, thereby establishing a positive feedback mechanism that maintains a continuously faster lifting of the fog top. During P2, the fog-top lifting is suppressed by warm advection and surface warming (see Ding et al., 2026), resulting in a shallower fog-top layer across all ARI conditions compared to P1 (Fig. 3a_ii). Although the radiative cooling rate, aerosol hygroscopic growth, and number of activated droplets within the fog-top layer in WetARI remain slightly higher than in the other ARI cases, their relative differences are significantly reduced compared to P1. Meanwhile, as the fog optical thickness increases, longwave radiative cooling near the fog top is enhanced relative to P1, leading to stronger negative buoyancy, which generates low-level turbulent mixing and contributes to vertical development of the mixed layer (Fig. 3c_ii). The mixing intensity follows WetARI > NoARI > DryARI, and the enhanced turbulence leads to a relatively homogeneous redistribution of fog droplets and liquid water within the lower layer (Fig. 3g_ii), thereby reducing the vertical gradient of the longwave radiative flux (Fig. 3d_ii), which is thus negatively correlated with mixing intensity. In contrast, differences in aerosol hygroscopic growth within the mixed layer among the three simulations are minor (Fig. 3h_ii), and their contribution to the differences in longwave radiative cooling is negligible. As a result, the supersaturation, number of activated particles, and liquid water content within the mixed layer show the same pattern as the longwave radiation gradient, i.e., WetARI < NoARI < DryARI (Fig. 3e_ii, 3f_ii and 3g_ii, respectively). During P2, the LWC at the fog-top layer in WetARI remains higher than in the other simulations but this is partly offset by a reduced LWC in the lower layer (Fig. 3g_ii), causing the LWP and τ across all simulations to become comparable. At some occurrences, the LWP and τ in the WetARI case even become the lowest (Fig. 2b). This indicates that in P2, the overall optical properties of the fog are no longer primarily dominated by the fog-top processes as in P1, but are instead more influenced by the vertical redistribution of droplets and liquid water in the mixed layer. During P3, when there is no warm-air advection aloft, the fog-top layer develops vertically once again (Fig. 3a_iii). In WetARI, a positive feedback mechanism driven by high aerosol hygroscopic growth, increased activation, and strong longwave radiative cooling, leads to a pronounced vertical growth of the fog-top layer, resulting in a significantly higher total LWP and τ compared to the NoARI and DryARI simulations. It is also noted that, although the differences in LWC between NoARI and DryARI at individual heights remain relatively small, the substantial increase in fog geometric thickness makes the vertically integrated quantities more sensitive to these LWC differences. Consequently, the contrast in LWP and τ between these two scenarios also becomes more pronounced during P3 than during P1 and P2 (Fig. 2b, c).

https://doi.org/10.5194/egusphere-2026-6876
Preprint. Discussion started: 12 November 2026
© Author(s) 2026. CC BY 4.0 License.

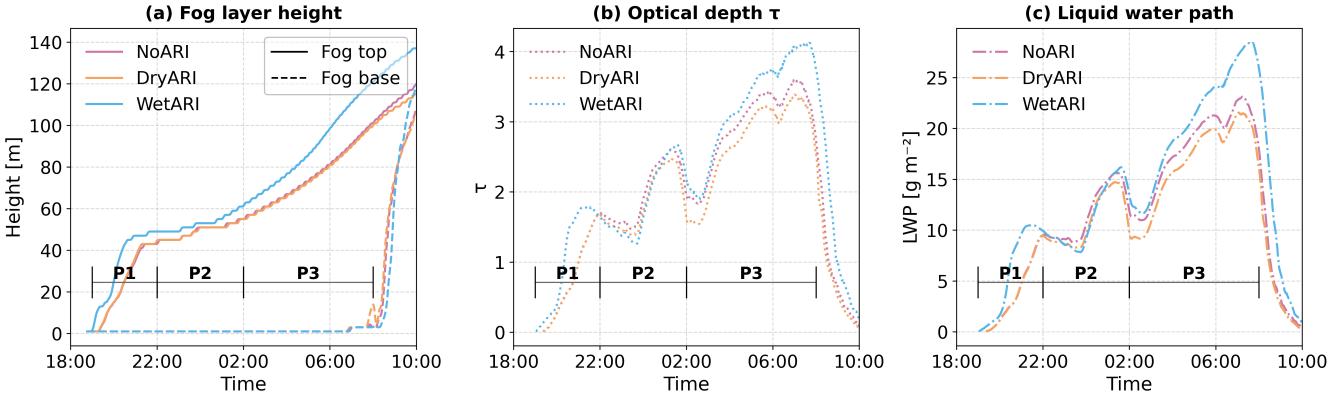


Figure 2. Temporal evolution of horizontally-averaged vertical fog properties in the reference simulations with different ARI representations: (a) fog layer height, (b) optical thickness (τ) and (c) liquid water path (LWP).

https://doi.org/10.5194/egusphere-2026-6876
Preprint. Discussion started: 12 November 2026
© Author(s) 2026. CC BY 4.0 License.

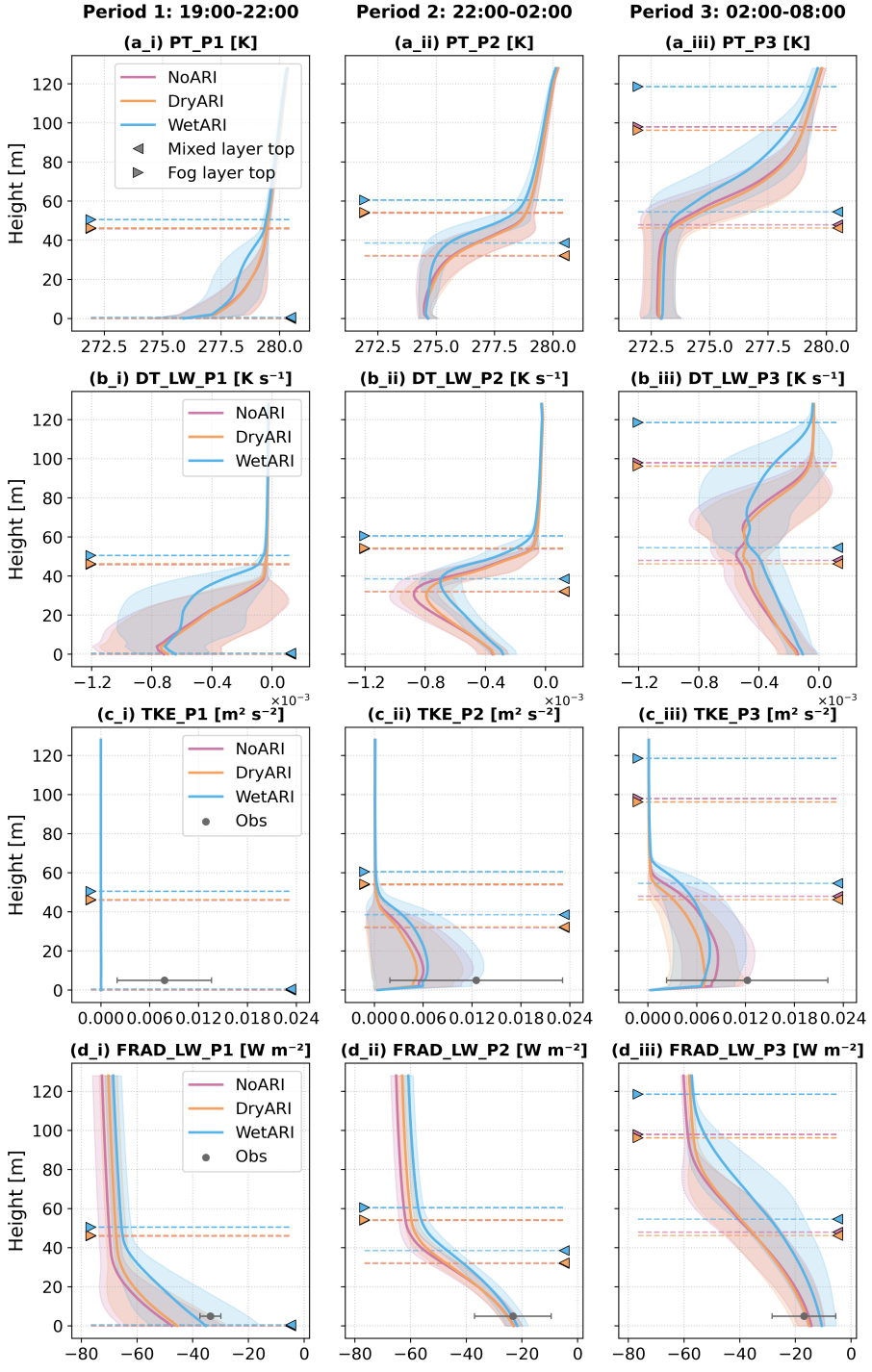


Figure 3. Vertical profiles of horizontally-averaged (a) potential temperature (PT), (b) longwave radiative rate (DT_LW), (c) turbulent kinetic energy (TKE) and (d) net longwave radiation flux (FRAD_LW) for the different reference simulations during the specified fog periods P1, P2, and P3 (see main text for further explanations). Solid lines indicate mean values and shaded areas indicate ±1 SD. Near-surface observed mean values are shown as gray dots, with error bars indicating ±1 SD. Left and right triangle markers with dashed lines indicate the mixed-layer height and fog-top height, respectively. Each column represents the same period.

https://doi.org/10.5194/egusphere-2026-6876
Preprint. Discussion started: 12 November 2026
© Author(s) 2026. CC BY 4.0 License.

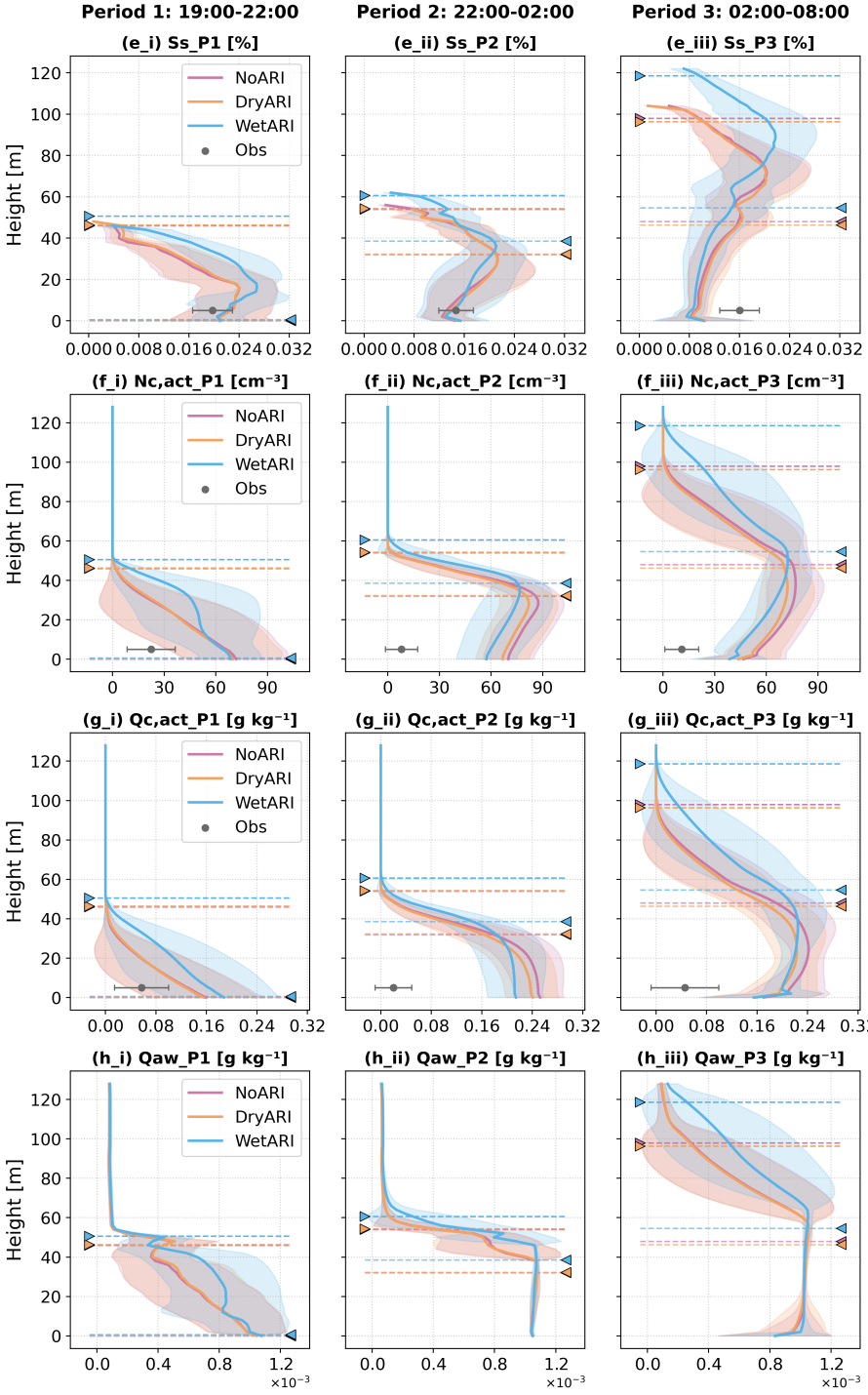


Figure 3. (Continued) Vertical profiles of horizontally-averaged (e) supersaturation (Ss), (f) number concentration of activated droplets ($N_{c,act}$), (g) liquid mixing ratio of activated droplets ($Q_{c,act}$), and (h) mixing ratio of aerosol water uptake (Q_{aw}) in the different reference simulations during the specified fog periods P1, P2, and P3 (see main text for further explanations). Solid lines indicate mean values and shaded areas indicate ±1 SD. Near-surface observed mean values are shown as gray dots, with error bars indicating ±1 SD. Left and right triangle markers with dashed lines indicate the mixed-layer height and fog-top height, respectively. Each column represents the same period.

https://doi.org/10.5194/egusphere-2026-6876
Preprint. Discussion started: 12 November 2026
© Author(s) 2026. CC BY 4.0 License.

Examining the near-surface fog properties, including fog lifetime, all three simulations reproduce the observed temporal evolution of the total number concentration of droplets larger than 2 μm in diameter reasonably well (Fig. 4a). However, due to limitations of the bulk microphysics scheme in representing the size distribution of large aerosol particles and their hygroscopic growth properties (see also discussion in Ding et al., 2026), the systematic overestimation of activated droplet number and liquid water content is not improved by including dry or wet ARI (Fig. 4b, 3f, 3g). In the early stages of fog formation, the WetARI case exhibits a higher near-surface radiative cooling rate than the other ARI simulations (Fig. 5d). This results in earlier droplet activation and fog onset (Fig. 4d) compared to the other two simulations. During the mature stages (P2 and P3), however, the radiative cooling rate in WetARI becomes relatively lower (Fig. 5d), most likely due to the enhanced turbulent mixing (Fig. 3c_ii, 3g_iii), leading to lower droplet number and liquid water content (Fig. 4a, 4b). The differences between NoARI and DryARI are small, mainly because the impacts of the dry aerosol components on longwave radiation are negligible (Fig. S1a). After sunrise, the shortwave radiation reaching the surface is substantially lower in WetARI compared to the other simulations, which also is in better agreement with observations. In contrast, both NoARI and DryARI significantly overestimate the surface net shortwave radiation, with NoARI exhibiting the largest bias (Fig. 5b); a similar pattern can also be found for the total net radiation (Fig. 5c). The difference between WetARI and the other two reference simulations can be attributed to two effects, which both increase the attenuation of shortwave radiation: first, the enhanced fog optical thickness due to increased aerosol activation; second, the radiative effects associated with aerosol hygroscopic growth. In the reference simulations, the fully coupled aerosol–radiation–cloud interactions do not allow isolating the contribution of ARI to shortwave radiation. However, results from the idealized experiments (Sect. S2) indicate that there is a slight increase in BC absorption in WetARI compared with DryARI due to the hygroscopic growth (the κ value for BC is 0.01 in MIMICA); meanwhile, the water uptake by highly hygroscopic sulfate and sea salt leads to a strong enhancement in shortwave scattering (Fig. S1h). Given that sulfate and sea salt dominate the aerosol mixture for the observed case, their attenuating effect on shortwave radiation far outweighs the enhanced BC absorption, so that the net direct radiative effect of aerosol water uptake is to further reduce the shortwave radiation reaching the surface. Consequently, the near-surface radiative heating rate under WetARI is lower and droplet evaporation is weaker, which leads to delayed fog dissipation relative to the other two simulations (Fig. 4e).

Overall, the total fog duration time and net surface radiation budget simulated in the WetARI case agree well with observations (Fig. 4e, 5c). Still, both the formation and the dissipation times are slightly delayed. This discrepancy may arise from uncertainties in the prescribed surface forcing, as the model uses the observed temperature at 3.5 m. Under nocturnal stable conditions, the surface is typically colder and shows greater temporal variability than the air above, which could introduce a temporal lag in the simulated fog life cycle relative to observations, as shown by (Ding et al., 2026). Furthermore, the net surface longwave radiation after sunrise is markedly higher in the model than in the observations (Fig. 5a). The observed net longwave radiation even becomes positive for a short time, which could indicate that a relatively warm low-level cloud was present above the model domain after fog dissipation. An additional sensitivity simulation, where we introduced the radiative properties of a low-level cloud based on the mean LWC profile from ERA5 during the fog period (Fig. S4), supports this assumption (Fig. S5).

https://doi.org/10.5194/egusphere-2026-6876
Preprint. Discussion started: 12 November 2026
© Author(s) 2026. CC BY 4.0 License.

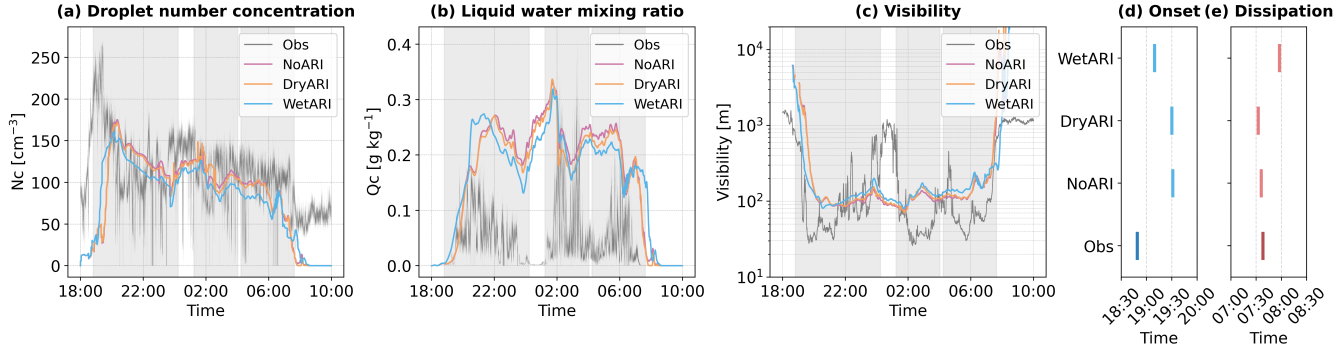


Figure 4. Near-surface time series of (a) total droplet number concentration, (b) liquid water mixing ratio, (c) visibility (parameterized using Eq. (3), considering both hydrated droplets and activated droplets), (d) fog onset on Feb 18 and (e) fog dissipation time on Feb 19 from observations (Obs) and simulations with varied ARI for the whole fog event. Gray shading highlights the fog periods identified from observed visibility.

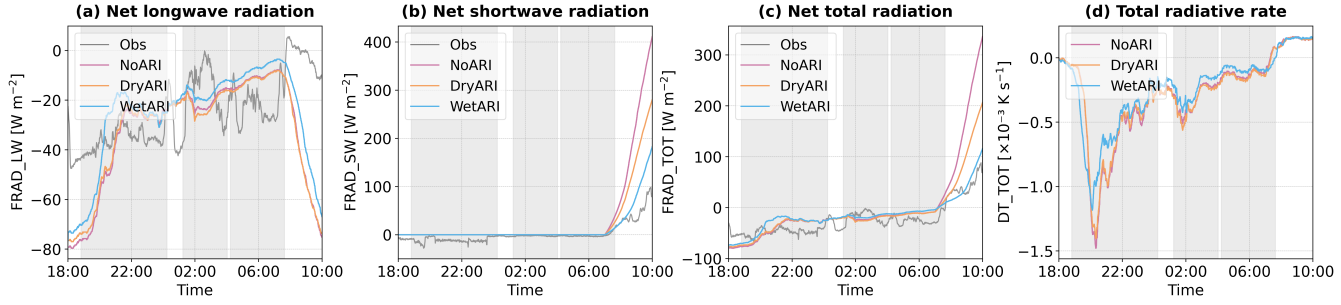


Figure 5. Near-surface time series of (a) net longwave radiation flux (FRAD_LW) and (b) net shortwave radiation flux (FRAD_SW), (c) net total radiation flux (FRAD_TOT) and (d) total radiative rate (DT_TOT) in observations (Obs) and reference simulations.

3.2 Sensitivity to aerosol loading

Increasing N_a consistently leads to earlier fog formation, delayed fog dissipation, and thus prolonged fog duration (Fig. 6). However, all model configurations show pronounced nonlinearities, with varying sensitivities among the three ARI conditions. This also suggests that models with different or no representation of ARI may show different sensitivities to changes in aerosol number concentrations.

In NoARI and DryARI, the earlier fog formation with increasing N_a is primarily caused by a visibility reduction through the increased number concentration of hydrated particles (Fig. 7g and 7a for NoARI, and Fig. 7h and 7b for DryARI, respectively, see also discussion in Ding et al., 2026). Note that the onset of fog is determined by the visibility criterion (Eq. 3), which considers both hydrated aerosols and activated droplets. In contrast, the radiative cooling rate remains relatively unchanged (Fig. 7d and Fig. 7e, respectively). When N_a increases to approximately 15,000 cm^{-3}, the earlier fog onset compared to the reference N_a stabilizes and occurs about 20 min earlier (Fig. 6a). However, in the WetARI case, the fog consistently starts earlier for each increase in N_a, and begins about 50 minutes earlier in the highest N_a case compared to the reference (Fig. 6a).

https://doi.org/10.5194/egusphere-2026-6876
Preprint. Discussion started: 12 November 2026
© Author(s) 2026. CC BY 4.0 License.

For WetARI, in addition to reducing visibility, the hydrated aerosols increase the longwave radiative cooling rate, which leads to an earlier droplet activation and earlier fog onset (Fig. 7f). The earlier droplet activation causes a feedback loop with even more cooling, more condensation, and an optically thicker fog (Fig. 7i, 7l and 7c).

Fog dissipation also shows a clear response to increasing N_a. In NoARI, the fog dissipation time is delayed by approximately 5 min for every 5,000 cm^{-3} increase in N_a (Fig. 6b, 8a). In DryARI, the response is weaker than in NoARI and stabilizes at concentrations higher than 15,000 cm^{-3} (Fig. 6b, 8b). The WetARI simulations consistently produce later fog dissipation than the other ARI experiments across the entire N_a range. However, the sensitivity to N_a is slightly weaker than in NoARI and DryARI and converges after N_a = 10,000 cm^{-3} (Fig. 6b). The reason is most likely a weakening of the decrease in the droplet sedimentation rate at higher N_a (Ding et al., 2026) as well as a nonlinear response in the attenuation in shortwave radiation. As N_a increases, the optical thickness of the fog layer increases, leading to more attenuation of shortwave radiation, which reduces near-surface radiative heating and suppresses droplet evaporation, as discussed in Sect. 3.1. However, when the fog layer becomes sufficiently optically thick, the attenuation of shortwave radiation becomes insensitive to further increases in N_a (Fig. 8o).

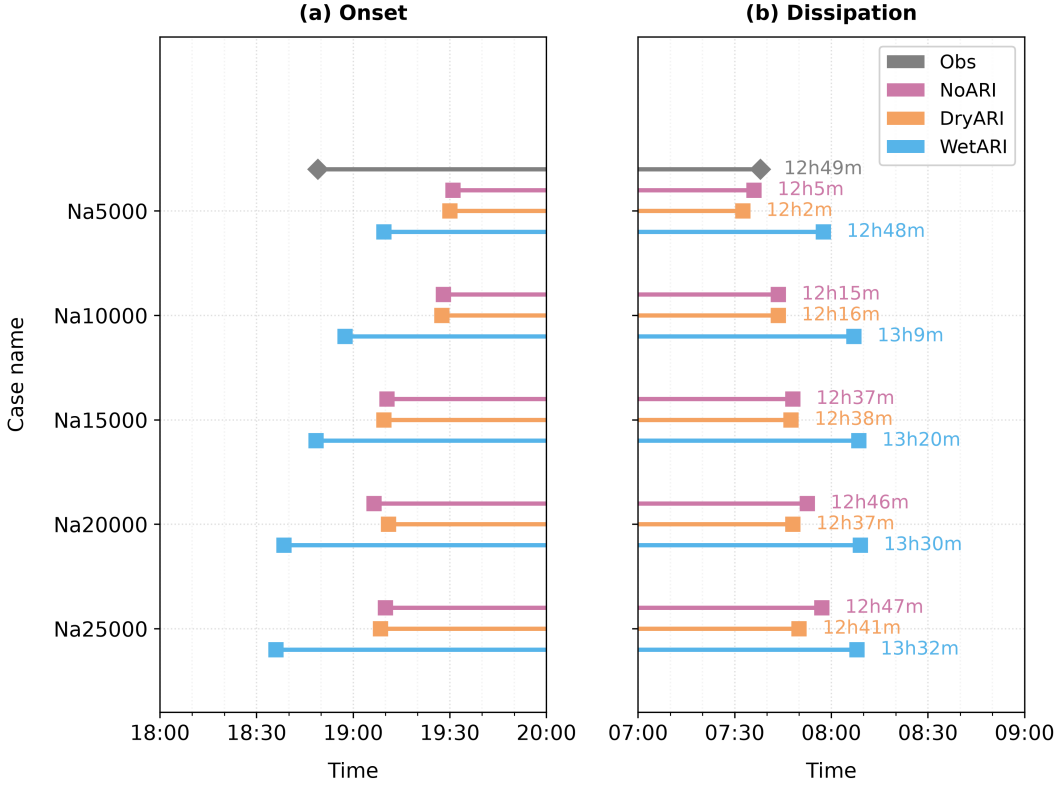


Figure 6. Time of (a) fog onset and (b) dissipation in observations (Obs) and sensitivity tests to aerosol loading (N_a) for the different ARI simulations (see Table. 2). Text labels in panel (b) indicate corresponding fog durations.

https://doi.org/10.5194/egusphere-2026-6876
Preprint. Discussion started: 12 November 2026
© Author(s) 2026. CC BY 4.0 License.

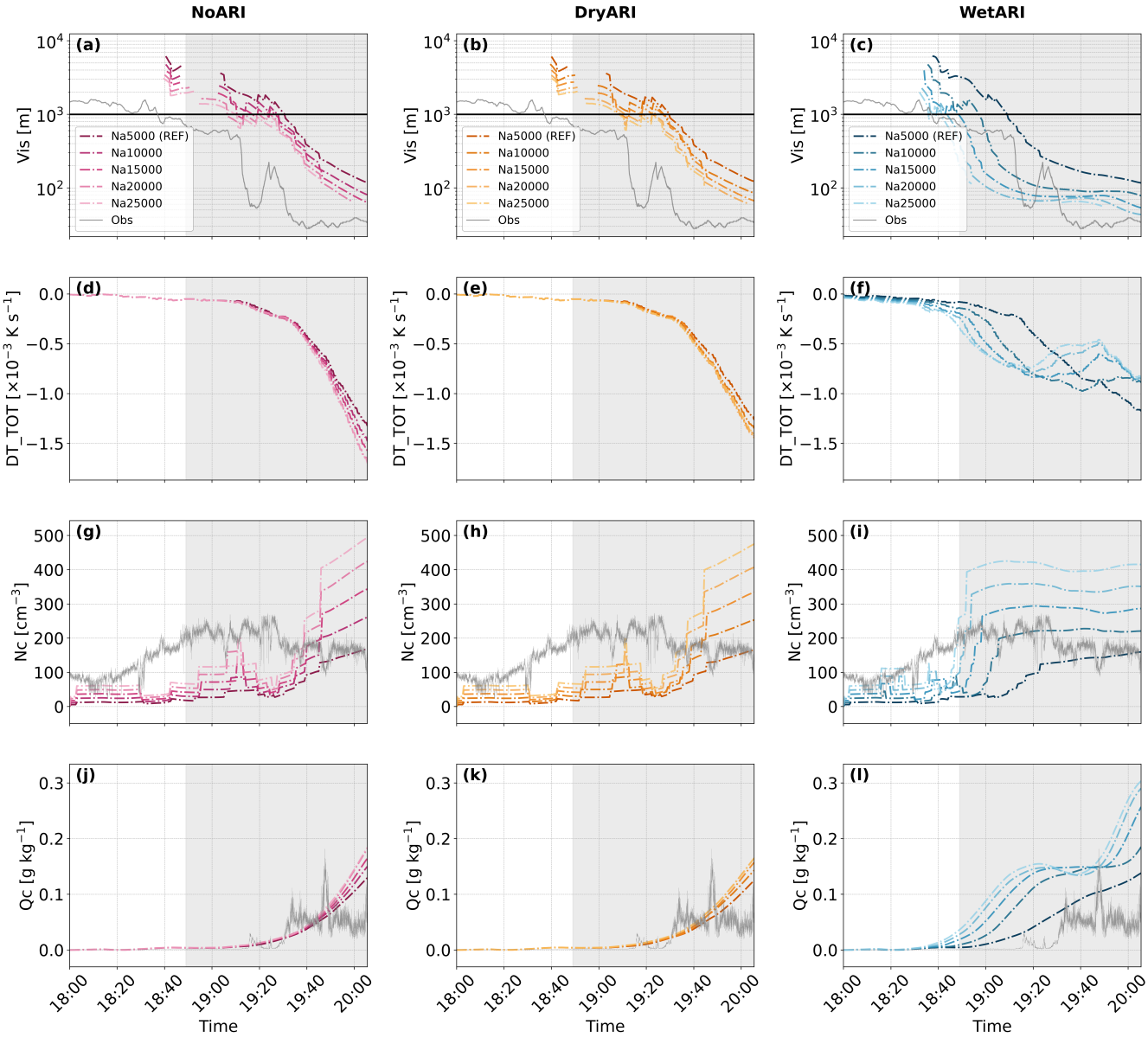


Figure 7. Temporal evolution of near-surface properties during fog formation for different N_a and ARI scenarios. The columns correspond to the NoARI, DryARI, and WetARI scenarios, respectively. Darker shades correspond to lower N_a, ranging from 5,000 to 25,000 cm^{-3}. From top to bottom, the panels show (a–c) visibility (Vis), (d–f) total radiative rate (DT_TOT), (g–i) total droplet number concentration (N_c), and (j–l) liquid water mixing ratio (Q_c). Gray shading indicates the observed fog periods, and gray curves represent the observed time series. Horizontal black lines in the visibility panels indicate the 1-km threshold.

https://doi.org/10.5194/egusphere-2026-6876
Preprint. Discussion started: 12 November 2026
© Author(s) 2026. CC BY 4.0 License.

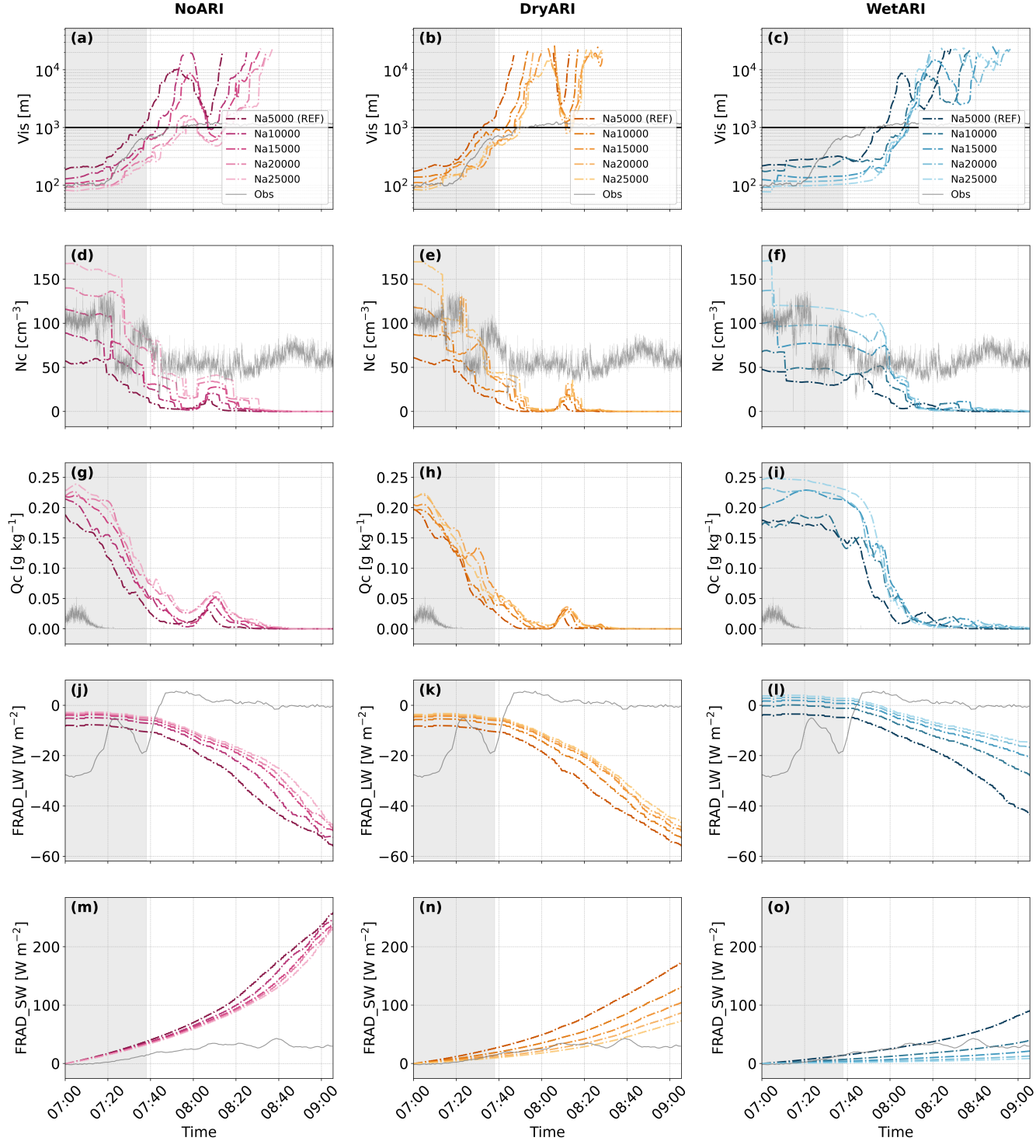


Figure 8. Same as Fig. 7, but for fog dissipation. From top to bottom, the panels show (a–c) visibility (Vis), (d–f) total droplet number concentration (N_c), (g–i) liquid water mixing ratio (Q_c), (j–l) net longwave radiation flux (FRAD_LW), and (m–o) net shortwave radiation flux (FRAD_SW).

https://doi.org/10.5194/egusphere-2026-6876
Preprint. Discussion started: 12 November 2026
© Author(s) 2026. CC BY 4.0 License.

In terms of the vertical fog properties, the geometric height, optical depth (τ) and LWP of the fog layer generally increase with N_a across all ARI scenarios, but the magnitude of the response differs substantially (Fig. 9). The following discussion refers to the mean relative changes averaged over the common fog period across the different N_a levels. For NoARI, the increase in fog-top height with increasing N_a is limited, with a maximum of 7.3% (Fig. 9a), and a corresponding increase in τ and LWP of 64.3% and 55.7%, respectively (Fig. 9b, 9c). This result confirms that in the absence of aerosol radiative effects, the enhanced optical depth and LWP with higher N_a mainly result from an increase in the concentration of activated droplets and hydrated particles, rather than from a substantial increase in the fog geometric thickness. In DryARI, the response of the fog vertical structure to N_a is the weakest among the three scenarios: the maximum difference is less than 4.3% and the corresponding increases in τ and LWP are only 37.2% and 28.2%, respectively (Fig. 9b, 9c). This is mainly attributed to the weakest longwave radiation flux gradient in DryARI, which limits radiative cooling, associated negative buoyancy and fog layer thickening (see also Sect. 3.1). In contrast, in WetARI, a strong positive feedback between aerosol hygroscopic growth, longwave radiative cooling, and droplet activation promotes vertical development of the fog-top layer. At the same time, turbulent mixing within the mixed layer is the most pronounced among the three scenarios (see also Sect. 3.1). These two factors together increase the sensitivity of the fog vertical structure to N_a. At N_a = 10,000 cm^{-3}, the increase in fog-top height, τ, and LWP relative to the reference is 15.5%, 36.5%, and 37.0%, respectively. When N_a = 25,000 cm^{-3}, the corresponding values reach 42.4%, 90.0%, and 91.3%, respectively (Fig. 9a, 9b,and 9c), which for all variables is substantially stronger compared to NoARI and DryARI.

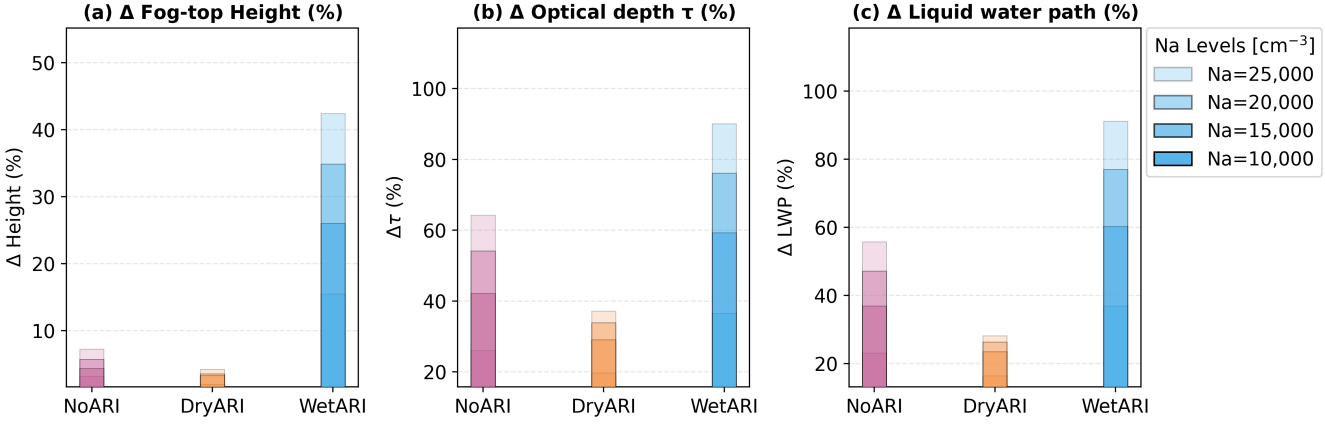


Figure 9. Temporal mean relative changes in (a) fog-top height, (b) optical depth (τ), and (c) liquid water path (LWP) compared to the corresponding reference simulations (N_a = 5,000 cm^{-3}), averaged over the overlapping fog periods, for the different ARI simulations. Lighter bar shading indicates higher N_a.

3.3 Sensitivity to chemical composition

For all ARI scenarios, increasing κ promotes aerosol hygroscopic growth (Fig. 10c) and droplet activation, leading to a higher total droplet number concentration, liquid water content, and stronger in-fog extinction (Fig. 10a, 10b and Fig. S7, respectively). Accordingly, fog duration is prolonged (Fig. 10f), mostly due to an earlier onset, with WetARI showing the most pronounced change (Fig. 10d). The stronger response is not only due to the enhanced aerosol hygroscopic growth, as in the other ARI cases,

https://doi.org/10.5194/egusphere-2026-6876
Preprint. Discussion started: 12 November 2026
© Author(s) 2026. CC BY 4.0 License.

but also a stronger longwave radiative cooling by the wet aerosols, which leads to enhanced droplet activation (Fig. S7l, S7i). Fog dissipation is generally delayed with increasing κ, except in NoARI (Fig. 10e). The highest sensitivity is again found in WetARI, where the increase in κ leads to a markedly higher fog optical depth, followed by a substantially weakened near-surface radiative heating and droplet evaporation after sunrise (Fig. S8l).

In contrast, variations in the BC content, within the range constrained by the FAIRARI observations, generate a small impact on fog properties (Fig. 11). Changes in fog onset and dissipation are generally smaller than 5 minutes for all ARI simulations (Fig. 11d, 11e). This is primarily attributed to the relatively small BC content and variations that were observed during the campaign (Fig. S2a). In DryARI and WetARI, increased BC content slightly enhances shortwave heating, but this effect is about two orders of magnitude weaker compared to the longwave cooling rate (Fig. 11a, 11b). Moreover, the relatively short daytime fog period limits the potential for any significant shortwave radiative response. Additional idealized experiments with BC volume fraction increased up to 50% also resulted in a weak response in fog microphysics and life cycle (not shown). Overall, in terms of chemical composition, aerosol hygroscopicity primarily controls fog processes for the observed case, while the radiative perturbations associated with BC content are weak.

https://doi.org/10.5194/egusphere-2026-6876
Preprint. Discussion started: 12 November 2026
© Author(s) 2026. CC BY 4.0 License.

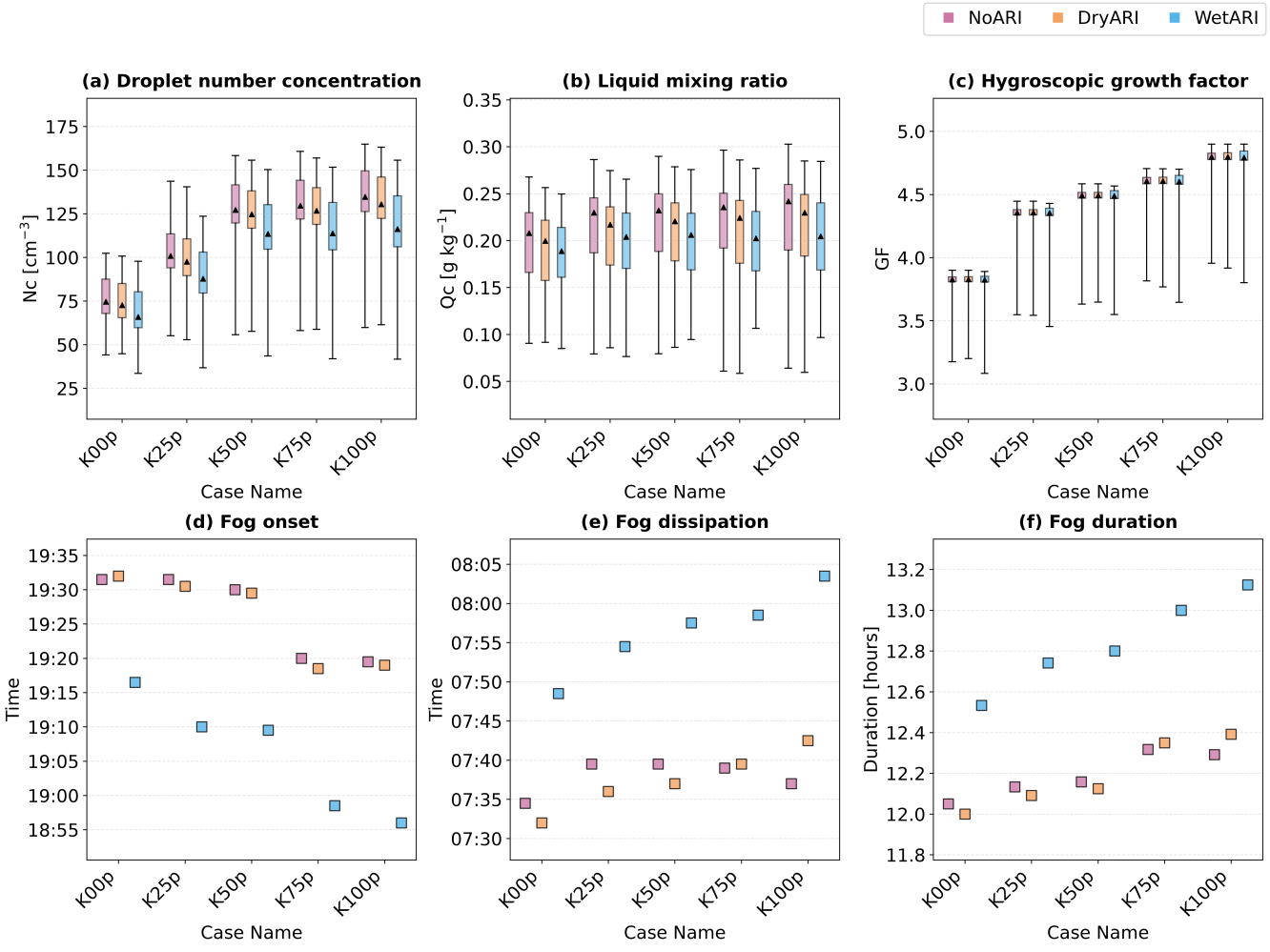


Figure 10. Statistics of near-surface fog properties in sensitivity experiments to aerosol hygroscopicity: (a) total droplet number concentration (N_c), (b) liquid mixing ratio (Q_c), (c) Hygroscopic growth factor (GF), (d) fog onset time, (e) fog dissipation time, and (f) fog duration. Boxes indicate the 25th-75th percentiles, whiskers the 5th-95th percentiles, and triangles the median.

https://doi.org/10.5194/egusphere-2026-6876
Preprint. Discussion started: 12 November 2026
© Author(s) 2026. CC BY 4.0 License.

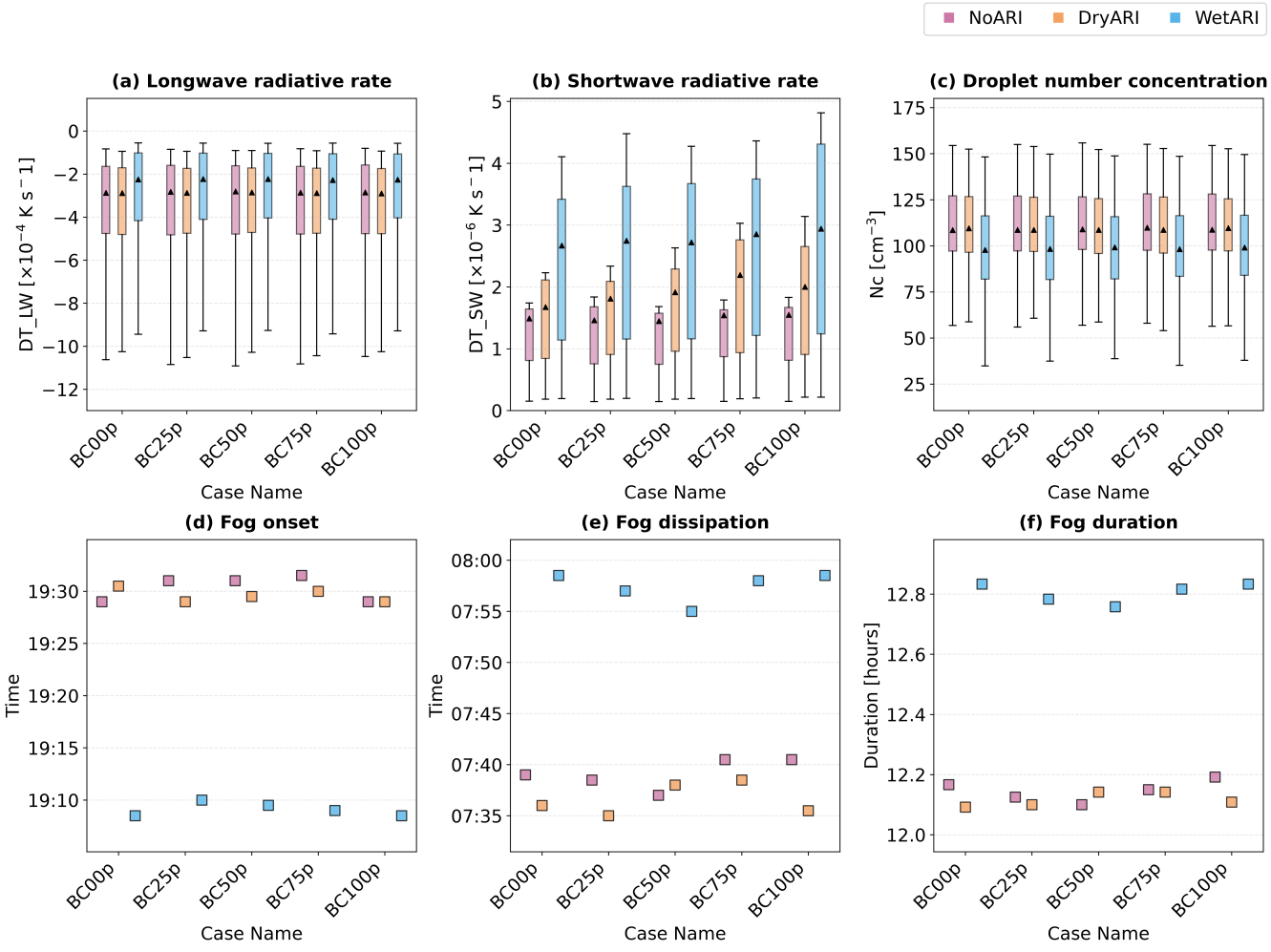


Figure 11. Statistics of near-surface fog properties in sensitivity experiments to BC content: (a) longwave radiative rate (DT_LW), (b) shortwave radiative rate (DT_SW) during daytime fog periods when DT_SW > 0, (c) total droplet number concentration (N_c), (d) fog onset time, (e) fog dissipation time and (f) fog duration. Boxes indicate the 25th-75th percentiles, whiskers the 5th-95th percentiles, and triangles the median.

4 Summary and conclusions

In this study, large-eddy simulation has been used to investigate how aerosol-radiation interactions (ARI) from aerosols that are considered to be dry ("dry ARI") or wet ("wet ARI") in the radiation calculations, respectively, affect the life cycle of an observed case of wintertime radiation fog in the Po Valley, Italy. We find that wet ARI have a substantially larger impact on the formation and evolution of the fog than dry ARI, as the aerosol water significantly enhances longwave radiative cooling, promoting droplet activation at the early stages of fog formation and generating a positive feedback loop through further longwave cooling. Consequently, wet ARI substantially increases the fog-top lifting rate, the optical depth of the fog, and the

https://doi.org/10.5194/egusphere-2026-6876
Preprint. Discussion started: 12 November 2026
© Author(s) 2026. CC BY 4.0 License.

turbulent mixing during the mature stage of the fog. At sunrise, the increased fog optical depth with wet ARI also reduces near-surface warming and delays fog dissipation. Overall, the fog lifetime increases by more than 40 minutes when wet ARI are considered compared to without any ARI. In contrast, the effect of dry ARI on fog properties and evolution is relatively weak for the simulated case. Including wet ARI also results in the best agreement with observed fog duration and near-surface radiative fluxes; when no ARI or only dry ARI are considered, the fog duration is underestimated by more than 40 minutes. Near-surface net radiative fluxes are also overestimated, particularly at sunrise when the fog dissipates. Our results indicate that an explicit consideration of aerosol hygroscopic growth and associated radiative effects, particularly in the longwave spectrum, is important for accurately reproducing the radiative budget, vertical structure, and life cycle of radiation fog.

An increase in the aerosol number concentration (N_a) generally prolongs fog duration, but the sensitivity is nonlinear and depends on whether wet ARI are considered or not. Overall, the sensitivity of the fog duration is considerably stronger when wet ARI are considered compared to only dry ARI or no ARI. With no ARI, and as shown in Ding et al. (2026), the fog forms earlier with increasing N_a as the increased number of hydrated aerosols decreases the visibility. The fog dissipation is also delayed due to a reduction in the sedimentation rate of the activated droplets. With dry ARI, there is no substantial impact on the radiative fluxes, and the results are similar to when no ARI are considered. The least pronounced response in fog geometric height and optical depth to N_a also occurs in dry ARI where the vertical gradient in longwave radiation and turbulent mixing is the weakest. When wet ARI are considered, increasing N_a strengthens the longwave radiative cooling at fog onset, which enhances droplet activation compared to with no ARI, resulting in a higher sensitivity of the fog formation and vertical development to N_a. Fog dissipation is also further delayed with increasing N_a when wet ARI are considered. In addition to the reduced droplet sedimentation rates, the fog becomes optically thicker with higher N_a, which dampens the near-surface warming and droplet evaporation at sunrise. However, the attenuation of the shortwave radiation tends to become insensitive to further increases in N_a once the fog is sufficiently optically thick (in our case at N_a = 10,000 cm^{-3}).

Increasing the hygroscopicity parameter (κ), within the range constrained by the FAIRARI observations, leads to higher droplet number concentrations and liquid water content, generally advancing fog formation and delaying its dissipation. Similar to increasing N_a, this effect is more pronounced when wet ARI are considered compared to with no ARI or dry ARI. Variations in the BC content, however, only have a limited influence on the fog microphysics and life cycle, regardless of whether wet or dry ARI are considered. The reason is that even though the increasing BC content enhances shortwave radiation absorption, its radiative effect is substantially smaller than the longwave cooling effect from changes in the liquid water during the fog period. Therefore, for the present case, BC content is not a critical factor governing the fog evolution.

Several limitations remain in this study. First, in our model, aerosol radiative effects are represented under the assumption of homogeneous internal aerosol mixing, without accounting for any core–shell structures that may occur in the real atmosphere (Schwarz et al., 2008; Kim et al., 2008; Li et al., 2016). Particularly for BC-containing particles, coatings may result in absorption enhancement and modify scattering properties, thereby introducing more complex nonlinearities in aerosol radiative effects. Second, due to the lack of observations of the vertical N_a distribution, we have assumed vertically uniform N_a profiles. One important aspect is also that we have forced our model with prescribed surface temperatures in order to isolate the radiative impact of the aerosols within the atmosphere. With an interactive surface scheme, ARI may affect surface cooling and warming

https://doi.org/10.5194/egusphere-2026-6876
Preprint. Discussion started: 12 November 2026
© Author(s) 2026. CC BY 4.0 License.

rates, which could be important when varying the aerosol concentration. These issues should be addressed in future studies to enhance our understanding of ARI in radiation fog.

Overall, this study provides a new research framework for understanding the role of ARI for radiation fog, highlighting the radiative effects of wet aerosols and demonstrating that incorporating only the radiative effects of activated droplets and dry aerosols in models may be insufficient. This study also has implications for understanding the observed decrease in fog occurrence in the Po Valley over recent decades, which has generally been attributed to reductions in CCN concentrations. Our results suggest that ARI and its response to changes in aerosol chemical composition should not be overlooked. ARI can substantially modify the radiative budget and the thermodynamic structure of the boundary layer, and may therefore modulate fog properties and lifetime on longer timescales.

https://doi.org/10.5194/egusphere-2026-6876
Preprint. Discussion started: 12 November 2026
© Author(s) 2026. CC BY 4.0 License.

Appendix A: Acronyms

Table A1. List of acronyms

Acronym	Description
ACI	aerosol-cloud interaction
ARI	aerosol-radiation interaction
BC	black carbon
DT_LW	longwave radiative rate
DT_SW	shortwave radiative rate
DT_TOT	total radiative rate
FAIRARI	Fog and Aerosol InteRAction Research Italy
FRAD_LW	net longwave radiation flux
FRAD_SW	net shortwave radiation flux
FRAD_TOT	net total radiation flux
HGF	hygroscopic growth factor
LES	Large Eddy Simulation
LST	Local Standard Time
LWC	liquid water content
LWP	liquid water path
MIMICA	MISU-MIT Cloud and Aerosol model
OA	organic aerosol
PT	potential temperature
RH	relative humidity
SALT	sea salt
SPC	San Pietro Capofiume
SULF	sulfate
TKE	turbulent kinetic energy
Vis	visibility

https://doi.org/10.5194/egusphere-2026-6876
Preprint. Discussion started: 12 November 2026
© Author(s) 2026. CC BY 4.0 License.

Code and data availability. The sounding data for San Pietro Capofiume are provided by the University of Wyoming Atmospheric Science Radiosonde Archive (https://weather.uwyo.edu/upperair/sounding.shtml). Aerosol data from the FAIRARI campaign are available through the Data Center of the Bolin Center for Climate Research (https://bolin.su.se/data/fairari-2021-2022). The MIMICA model code can be accessed at https://bitbucket.org/matthiasbrakebusch/mimicav5/src/master.

Author contributions. Conceptualization: HD, SD, PZ, IR and AMLE; Data curation: HD, AN, RR, FM and AMLE; Formal analysis: HD, AN, RR, FM, KM and ABP; Funding acquisition: SD, IR and AMLE; Investigation: HD, ABP, NM, AN, RR, FM, LH, KM, SD, AL, CM, PZ, IR and AMLE; Methodology: HD, ABP, NM, AN, RR, FM, LH, KM, SD, CM, PZ, IR and AMLE; Project administration: HD, SD, CM, PZ, IR and AMLE; Resources: SD, AL, CM, PZ, IR and AMLE; Software: HD, ABP, NM and AMLE; Supervision: PZ, IR and AMLE; Validation: HD, ABP and NM; Visualization: HD, ABP and AMLE; Writing - Original Draft: HD, AN, PZ, IR and AMLE; Writing - Review & Editing: HD, AN, RR, FM, LH, KM, SD, ABP, NM, PZ, IR and AMLE.

Competing interests. Some authors are members of the editorial board of journal Atmospheric Chemistry and Physics.

Acknowledgements. Financial support from the European Union's Horizon 2020 research and innovation programme (Project FORCeS under Grant Agreement 821205), European Research Council (Consolidator Grant INTEGRATE 865799) and Horizon Europe programme (Project CERTAINTY under Grant Agreement 101137680) is gratefully acknowledged. We also acknowledge financial support from the Knut and Alice Wallenberg Foundation through grants for project AtmoRemove (No. 2015.0162), AtmoCLOUD (No. 2021.0169 and No. 2021.0298), and CLIVE (No. 2022.0104), as well as from Goran Gustafssons stiftelse and the Swedish Research Council (No. 2020–04158). The computations and data handling in MIMICA were enabled by resources provided by the National Academic Infrastructure for Supercomputing in Sweden (NAISS), partially funded by the Swedish Research Council (No. 2022-06725).

https://doi.org/10.5194/egusphere-2026-6876
Preprint. Discussion started: 12 November 2026
© Author(s) 2026. CC BY 4.0 License.

References

Anurose, T. J., Jayakumar, A., Sandhya, M., Gordon, H., Aryasree, S., Mohandas, S., Bhati, S., and Prasad, V. S.: Unraveling the Mechanism of the Holes in the Blanket of Fog Over the Indo-Gangetic Plains: Are They Driven by Urban Heat Islands or Aerosol?, Geophysical Research Letters, 51, https://doi.org/10.1029/2023gl107252, 2024.

Arun, N., Sarangi, C., and Qian, Y.: Particulate Pollution Increases Fog Duration Over the Indo-Gangetic Plain, Geophysical Research Letters, 52, https://doi.org/10.1029/2024gl114095, 2025.

Baró Pérez, A., Diamond, M. S., Bender, F. A.-M., Devasthale, A., Schwarz, M., Savre, J., Tonttila, J., Kokkola, H., Lee, H., Painemal, D., and Ekman, A. M. L.: Comparing the simulated influence of biomass burning plumes on low-level clouds over the southeastern Atlantic under varying smoke conditions, Atmospheric Chemistry and Physics, 24, 4591–4610, https://doi.org/10.5194/acp-24-4591-2024, 2024.

Bergot, T.: Small-scale structure of radiation fog: a large-eddy simulation study, Quarterly Journal of the Royal Meteorological Society, 139, 1099–1112, https://doi.org/10.1002/qj.2051, 2013.

Bergot, T.: Large-eddy simulation study of the dissipation of radiation fog, Quarterly Journal of the Royal Meteorological Society, 142, 1029–1040, https://doi.org/10.1002/qj.2706, 2016.

Bond, T. C. and Bergstrom, R. W.: Light absorption by carbonaceous particles: An investigative review, Aerosol science and technology, 40, 27–67, https://doi.org/10.1080/02786820500421521, 2006.

Bond, T. C., Doherty, S. J., Fahey, D. W., Forster, P. M., Berntsen, T., DeAngelo, B. J., Flanner, M. G., Ghan, S., Kärcher, B., Koch, D., Kinne, S., Kondo, Y., Quinn, P. K., Sarofim, M. C., Schultz, M. G., Schulz, M., Venkataraman, C., Zhang, H., Zhang, S., Bellouin, N., Guttikunda, S. K., Hopke, P. K., Jacobson, M. Z., Kaiser, J. W., Klimont, Z., Lohmann, U., Schwarz, J. P., Shindell, D., Storelvmo, T., Warren, S. G., and Zender, C. S.: Bounding the role of black carbon in the climate system: A scientific assessment, Journal of Geophysical Research: Atmospheres, 118, 5380–5552, https://doi.org/10.1002/jgrd.50171, 2013.

Bott, A., Sievers, U., and Zdunkowski, W.: A radiation fog model with a detailed treatment of the interaction between radiative transfer and fog microphysics, Journal of Atmospheric Sciences, 47, 2153–2166, https://doi.org/10.1175/1520-0469(1990)047<2153:arfmwa>2.0.co;2, 1990.

Brenguier, J.-L., Burnet, F., and Geoffroy, O.: Cloud optical thickness and liquid water path–does the k coefficient vary with droplet concentration?, Atmospheric Chemistry and Physics, 11, 9771–9786, https://doi.org/10.5194/acp-11-9771-2011, 2011.

Contreras Osorio, S., Martín Pérez, D., Ivarsson, K.-I., Nielsen, K. P., de Rooy, W. C., Gleeson, E., and McAufield, E.: Impact of the Microphysics in HARMONIE-AROME on Fog, Atmosphere, 13, 2127, https://doi.org/10.3390/atmos13122127, 2022.

Decesari, S., Sowlat, M. H., Hasheminassab, S., Sandrini, S., Gilardoni, S., Facchini, M. C., Fuzzi, S., and Sioutas, C.: Enhanced toxicity of aerosol in fog conditions in the Po Valley, Italy, Atmospheric Chemistry and Physics, 17, 7721–7731, https://doi.org/10.5194/acp-17-7721-2017, 2017.

Di Antonio, L., Di Biagio, C., Foret, G., Formenti, P., Siour, G., Doussin, J.-F., and Beekmann, M.: Aerosol optical depth climatology from the high-resolution MAIAC product over Europe: differences between major European cities and their surrounding environments, Atmospheric Chemistry and Physics, 23, 12 455–12 475, https://doi.org/10.5194/acp-23-12455-2023, 2023.

Ding, A. J., Huang, X., Nie, W., Sun, J. N., Kerminen, V., Petäjä, T., Su, H., Cheng, Y. F., Yang, X., Wang, M. H., Chi, X. G., Wang, J. P., Virkkula, A., Guo, W. D., Yuan, J., Wang, S. Y., Zhang, R. J., Wu, Y. F., Song, Y., Zhu, T., Zilitinkevich, S., Kulmala, M., and Fu, C. B.: Enhanced haze pollution by black carbon in megacities in China, Geophysical Research Letters, 43, 2873–2879, https://doi.org/10.1002/2016gl067745, 2016.

https://doi.org/10.5194/egusphere-2026-6876
Preprint. Discussion started: 12 November 2026
© Author(s) 2026. CC BY 4.0 License.

Ding, H., Neuberger, A., Ranjan, R., Mattsson, F., Heikkinen, L., Mansour, K., Decesari, S., Mohr, C., Pérez, A. B., Mastroianni, N., Zieger, P., Riipinen, I., and Ekman, A. M. L.: The importance of aerosol and droplet microphysics for the properties and life cycle of radiation fog in the Po Valley, Atmospheric Chemistry and Physics, 26, 9721–9739, https://doi.org/10.5194/acp-26-9721-2026, 2026.

Ding, Q., Sun, J., Huang, X., Ding, A., Zou, J., Yang, X., and Fu, C.: Impacts of black carbon on the formation of advection–radiation fog during a haze pollution episode in eastern China, Atmospheric Chemistry and Physics, 19, 7759–7774, https://doi.org/10.5194/acp-19-7759-2019, 2019.

Egli, S., Thies, B., and Bendix, J.: A spatially explicit and temporally highly resolved analysis of variations in fog occurrence over Europe, Quarterly Journal of the Royal Meteorological Society, 145, 1721–1740, https://doi.org/10.1002/qj.3522, 2019.

Ekman, A. M. L., Wang, C., Ström, J., and Krejci, R.: Explicit simulation of aerosol physics in a cloud-resolving model: Aerosol transport and processing in the free troposphere, Journal of the atmospheric sciences, 63, 682–696, https://doi.org/10.1175/jas3645.1, 2006.

Elias, T., Dupont, J.-C., Hammer, E., Hoyle, C., Haeffelin, M., Burnet, F., and Jolivet, D.: Enhanced extinction of visible radiation due to hydrated aerosols in mist and fog, Atmospheric Chemistry and Physics, 15, 6605–6623, https://doi.org/10.5194/acp-15-6605-2015, 2015.

Fu, Q. and Liou, K.: Parameterization of the radiative properties of cirrus clouds, Journal of the atmospheric sciences, 50, 2008–2025, https://doi.org/10.1175/1520-0469(1993)050<2008:POTRPO>2.0.CO;2, 1993.

Fu, Q., Liou, K. N., Cribb, M. C., Charlock, T. P., and Grossman, A.: Multiple Scattering Parameterization in Thermal Infrared Radiative Transfer, Journal of the Atmospheric Sciences, 54, 2799–2812, https://doi.org/10.1175/1520-0469(1997)054<2799:mspiti>2.0.co;2, 1997.

Gao, Y., Zhang, M., Liu, Z., Wang, L., Wang, P., Xia, X., Tao, M., and Zhu, L.: Modeling the feedback between aerosol and meteorological variables in the atmospheric boundary layer during a severe fog–haze event over the North China Plain, Atmospheric Chemistry and Physics, 15, 4279–4295, https://doi.org/10.5194/acp-15-4279-2015, 2015.

Gu, Y., Farrara, J., Liou, K. N., and Mechoso, C. R.: Parameterization of cloud–radiation processes in the UCLA general circulation model, Journal of climate, 16, 3357–3370, https://doi.org/10.1175/1520-0442(2003)016<3357:pocpit>2.0.co;2, 2003.

Gultepe, I., Müller, M. D., and Boybeyi, Z.: A new visibility parameterization for warm-fog applications in numerical weather prediction models, Journal of applied meteorology and climatology, 45, 1469–1480, https://doi.org/10.1175/jam2423.1, 2006.

Hammer, E., Gysel, M., Roberts, G. C., Elias, T., Hofer, J., Hoyle, C. R., Bukowiecki, N., Dupont, J.-C., Burnet, F., Baltensperger, U., Hering, A. S., Jaffrezo, J. L., and Weingartner, B.: Size-dependent particle activation properties in fog during the ParisFog 2012/13 field campaign, Atmospheric Chemistry and Physics, 14, 10 517–10 533, https://doi.org/10.5194/acp-14-10517-2014, 2014.

Hersbach, H., Bell, B., Berrisford, P., Biavati, G., Horányi, A., Muñoz Sabater, J., Nicolas, J., Peubey, C., Radu, R., Rozum, I., Schepers, D., Simmons, A., Soci, C., Dee, D., and Thépaut, J.-N.: ERA5 hourly data on pressure levels from 1940 to present, Copernicus climate change service (c3s) climate data store (cds), 10, 24 381, https://doi.org/10.24381/cds.bd0915c6, 2023.

Karlsson, L., Baccarini, A., Duplessis, P., Baumgardner, D., Brooks, I. M., Chang, R. Y., Dada, L., Dällenbach, K. R., Heikkinen, L., Krejci, R., Leaitch, W. R., Leck, C., Partridge, D. G., Salter, M. E., Wernli, H., Wheeler, M. J., Schmale, J., and Zieger, P.: Physical and Chemical Properties of Cloud Droplet Residuals and Aerosol Particles During the Arctic Ocean 2018 Expedition, Journal of Geophysical Research: Atmospheres, 127, https://doi.org/10.1029/2021jd036383, 2022.

Kim, D., Wang, C., Ekman, A. M. L., Barth, M. C., and Rasch, P. J.: Distribution and direct radiative forcing of carbonaceous and sulfate aerosols in an interactive size-resolving aerosol–climate model, Journal of Geophysical Research: Atmospheres, 113, https://doi.org/10.1029/2007jd009756, 2008.

https://doi.org/10.5194/egusphere-2026-6876
Preprint. Discussion started: 12 November 2026
© Author(s) 2026. CC BY 4.0 License.

Li, W., Sun, J., Xu, L., Shi, Z., Riemer, N., Sun, Y., Fu, P., Zhang, J., Lin, Y., Wang, X., Shao, L., Chen, J., Zhang, X., Wang, Z., and Wang, W.: A conceptual framework for mixing structures in individual aerosol particles, Journal of Geophysical Research: Atmospheres, 121, https://doi.org/10.1002/2016jd025252, 2016.

Maalick, Z., Kühn, T., Korhonen, H., Kokkola, H., Laaksonen, A., and Romakkaniemi, S.: Effect of aerosol concentration and absorbing aerosol on the radiation fog life cycle, Atmospheric Environment, 133, 26–33, https://doi.org/10.1016/j.atmosenv.2016.03.018, 2016.

Maronga, B. and Bosveld, F.: Key parameters for the life cycle of nocturnal radiation fog: a comprehensive large-eddy simulation study, Quarterly Journal of the Royal Meteorological Society, 143, 2463–2480, https://doi.org/10.1002/qj.3100, 2017.

Morrison, H. and Grabowski, W. W.: Comparison of bulk and bin warm-rain microphysics models using a kinematic framework, Journal of the atmospheric sciences, 64, 2839–2861, https://doi.org/10.1175/jas3980, 2007.

Morrison, H. and Grabowski, W. W.: Modeling supersaturation and subgrid-scale mixing with two-moment bulk warm microphysics, Journal of the Atmospheric Sciences, 65, 792–812, https://doi.org/10.1175/2007JAS2374.1, 2008.

Neuberger, A., Decesari, S., Aktypis, A., Andersen, H., Baumgardner, D., Bianchi, F., Busetto, M., Cai, J., Cermak, J., Dipu, S., Ekman, A. M. L., Fuzzi, S., Gramlich, Y., Haslett, S. L., Heikkinen, L., Joutsensaari, J., Kaltsonoudis, C., Kangasluoma, J., Krejci, R., Lupi, A., Marinoni, A., Matrali, A., Mattsson, F., Mohr, C., Nenes, A., Paglione, M., Pandis, S. N., Patel, A., Riipinen, I., Rinaldi, M., Steimer, S. S., Stolzenburg, D., Sulo, J., Vasilakopoulou, C. N., and Zieger, P.: From Molecules to Droplets: The Fog and Aerosol Interaction Research Italy (FAIRARI) 2021/22 Campaign, Bulletin of the American Meteorological Society, 106, E23–E50, https://doi.org/10.1175/bams-d-23-0166.1, 2025a.

Neuberger, A., Ranjan, R., Ding, H., Mattsson, F., Haberstock, L., Baumgardner, D., Decesari, S., Ekman, A. M. L., Hughes, D. D., Mohr, C., Paglione, M., Riipinen, I., Rinaldi, M., and Zieger, P.: Importance of hydrated aerosol particles for aerosol-fog relationships in the Italian Po Valley, EGUsphere[preprint], 2025, 1–38, https://doi.org/10.5194/egusphere-2025-5419, 2025b.

Nguyen, T. K. V., Zhang, Q., Jimenez, J. L., Pike, M., and Carlton, A. G.: Liquid Water: Ubiquitous Contributor to Aerosol Mass, Environmental Science amp; Technology Letters, 3, 257–263, https://doi.org/10.1021/acs.estlett.6b00167, 2016.

Noone, K. J., Ogren, J. A., Hallberg, A., Heintzenberg, J., Ström, J., Hansson, H.-C., Svenningsson, B., Wiedensohler, A., Fuzzi, S., Facchini, M. C., Arends, B. G., and Berner, A.: Changes in aerosol size- and phase distributions due to physical and chemical processes in fog, Tellus B, 44, 489–504, https://doi.org/10.3402/tellusb.v44i5.15563, 1992.

Onasch, T. B., Trimborn, A., Fortner, E. C., Jayne, J. T., Kok, G. L., Williams, L. R., Davidovits, P., and Worsnop, D. R.: Soot Particle Aerosol Mass Spectrometer: Development, Validation, and Initial Application, Aerosol Science and Technology, 46, 804–817, https://doi.org/10.1080/02786826.2012.663948, 2012.

Pauli, E., Cermak, J., Bendix, J., and Stier, P.: Synoptic Scale Controls and Aerosol Effects on Fog and Low Stratus Life Cycle Processes in the Po Valley, Italy, Geophysical Research Letters, 51, https://doi.org/10.1029/2024gl111490, 2024.

Petters, M. and Kreidenweis, S.: A single parameter representation of hygroscopic growth and cloud condensation nucleus activity, Atmospheric Chemistry and Physics, 7, 1961–1971, https://doi.org/10.5194/acp-7-1961-2007, 2007.

Petäjä, T., Järvi, L., Kerminen, V.-M., Ding, A., Sun, J., Nie, W., Kujansuu, J., Virkkula, A., Yang, X., Fu, C., Zilitinkevich, S., and Kulmala, M.: Enhanced air pollution via aerosol-boundary layer feedback in China, Scientific Reports, 6, https://doi.org/10.1038/srep18998, 2016.

Price, J.: Radiation fog. Part I: observations of stability and drop size distributions, Boundary-layer meteorology, 139, 167–191, https://doi.org/10.1007/s10546-010-9580-2, 2011.

Putaud, J. P., Cavalli, F., Martins dos Santos, S., and Dell'Acqua, A.: Long-term trends in aerosol optical characteristics in the Po Valley, Italy, Atmospheric Chemistry and Physics, 14, 9129–9136, https://doi.org/10.5194/acp-14-9129-2014, 2014.

https://doi.org/10.5194/egusphere-2026-6876
Preprint. Discussion started: 12 November 2026
© Author(s) 2026. CC BY 4.0 License.



Savre, J., Ekman, A. M. L., and Svensson, G.: Technical note: Introduction to MIMICA, a large-eddy simulation solver for cloudy planetary boundary layers, Journal of Advances in Modeling Earth Systems, 6, 630–649, https://doi.org/https://doi.org/10.1002/2013MS000292, 2014.

Schwarz, J. P., Spackman, J. R., Fahey, D. W., Gao, R. S., Lohmann, U., Stier, P., Watts, L. A., Thomson, D. S., Lack, D. A., Pfister, L., Mahoney, M. J., Baumgardner, D., Wilson, J. C., and Reeves, J. M.: Coatings and their enhancement of black carbon light absorption in the tropical atmosphere, Journal of Geophysical Research: Atmospheres, 113, https://doi.org/10.1029/2007jd009042, 2008.

Seifert, A. and Beheng, K. D.: A double-moment parameterization for simulating autoconversion, accretion and selfcollection, Atmospheric research, 59, 265–281, https://doi.org/10.1016/S0169-8095(01)00126-0, 2001.

Seifert, A. and Beheng, K. D.: A two-moment cloud microphysics parameterization for mixed-phase clouds. Part 1: Model description, Meteorology and atmospheric physics, 92, 45–66, https://doi.org/10.1007/s00703-005-0112-4, 2006.

Slater, J., Tonttila, J., McFiggans, G., Connolly, P., Romakkaniemi, S., Kühn, T., and Coe, H.: Using a coupled large-eddy simulation–aerosol radiation model to investigate urban haze: sensitivity to aerosol loading and meteorological conditions, Atmospheric Chemistry and Physics, 20, 11 893–11 906, https://doi.org/10.5194/acp-20-11893-2020, 2020.

Stokes, R. H. and Robinson, R. A.: Interactions in Aqueous Nonelectrolyte Solutions. I. Solute-Solvent Equilibria, The Journal of Physical Chemistry, 70, 2126–2131, https://doi.org/10.1021/j100879a010, 1966.

Stolaki, S., Haeffelin, M., Lac, C., Dupont, J.-C., Elias, T., and Masson, V.: Influence of aerosols on the life cycle of a radiation fog event. A numerical and observational study, Atmospheric Research, 151, 146–161, https://doi.org/10.1016/j.atmosres.2014.04.013, 2015.

Stull, R. B.: An Introduction to Boundary Layer Meteorology, Kluwer Academic Publishers, Dordrecht, https://doi.org/10.1007/978-94-009-3027-8, 1988.

Yan, S., Zhu, B., Zhu, T., Shi, C., Liu, D., Kang, H., Lu, W., and Lu, C.: The effect of aerosols on fog lifetime: Observational evidence and model simulations, Geophysical Research Letters, 48, e2020GL61 803, https://doi.org/10.1029/2020gl091156, 2021.